BNL-76860-2006-BC

H_2 Production and Fuel Cells

Xianqin Wang[1] and José A. Rodriguez[2]

[1]Pacific Northwest National Laboratory, Richland, WA 99352, USA
[2]Brookhaven National Laboratory, Upton, NY 11973, USA

To be published in "Synthesis, Properties and Applications of Oxide Nanomaterials"

June 2006

Chemistry Department

Brookhaven National Laboratory
P.O. Box 5000
Upton, NY 11973-5000
www.bnl.gov

DISCLAIMER

Chapter 21

H_2 Production and Fuel Cells

Xianqin Wang[1] and José A. Rodriguez[2]

[1]Institute for Interfacial Catalysis, Pacific Northwest National Laboratory, Richland, WA, 99352 (USA)

[2]Chemistry Department, Brookhaven National Laboratory, Upton, NY, 11973 (USA)

Table of Contents:

I. Introduction

The finding of new sources of energy is perhaps the most important problem that faces humanity today[1]. The crucial energy problem is caused by the decrease in fossil fuel reserves due to world population growth, technological developments and increasing energy demand; the global climate change due to the increase of carbon dioxide concentration from the burning of fossil fuels in the atmosphere; and the conflicts and wars due to fluctuations in energy prices, economic recessions, decrease in living standards and increase in unrest among countries.[2] The energy policy of the developed countries is directed by the need for a secure energy supply and by the wish for sustainable growth. Therefore, the new challenges are to create alternate fuels, clean the environment, deal with the causes of global warming, and keep us safe from toxic substances and infectious agents.[3]

There are many different kinds of alternate fuels: liquefied petroleum gas, natural gas, methanol, dimethylether, ethanol, bio-diesel, synfuel, and hydrogen.[4] Among these alternative fuels, hydrogen is a potential solution for satisfying many of our energy needs while reducing (and eventually eliminating) carbon dioxide and other greenhouse gas emissions[5,6,7,8]. In the early 1970s, the potential use of hydrogen was discussed at the beginning of the energy crisis. Nowadays, it is high on the political agenda and on the priorities of agencies funding research. Hydrogen is expected to play an important role in future energy scenarios, replacing to some degree fossil fuels and becoming the preferred portable energy carrier for vehicles and in stationary applications as well. Fuel cells will play a key role for both situations, as will be discussed below.

Hydrogen can be manufactured via a variety of routes as shown in Figure 1. Hydrogen, the most plentiful element available, can be extracted from water by electrolysis. One can imagine capturing energy from the sun and wind and/or from the depths of the earth to provide the necessary power for electrolysis. Alternative energy sources such as these are the promise for the future, but for now they are not feasible for the power needs across the globe. A transitional solution is required to convert certain hydrocarbon fuels to hydrogen.[9] Renewable energy sources such as hydraulic, solar, wind, geothermal, wave and solid waste energy can be used to generate hydrogen from hydrocarbons and/or water. The use of natural gas represents a partial solution because of its high content of hydrogen. Biomass may be converted into hydrogen via gasification or by pyrolysis, followed by liquid phase "reforming" at subcritical conditions. At present, nearly 95% of the hydrogen supply is produced from the reforming of crude oil, coal, natural gas, wood, organic wastes and biomass.[10] Hydrogen is manufactured today primarily by reacting steam with natural gas. This is the cheapest route, at least for the demand known today, and the process is highly efficient.[4]

Fuel cells play a key role for the use of hydrogen in stationary and mobile applications. A fuel cell is a device that uses hydrogen (or a hydrogen-rich fuel) and oxygen to cleanly and efficiently produce electricity by an electrochemical process with water and heat as by products. Fuel cells are unique in terms of the variety of their potential applications; they can provide energy for systems as large as a utility power station and as small as a laptop computer. Fuel cells have several benefits over conventional combustion-based technologies currently used in many power plants and passenger vehicles. They produce much smaller quantities of greenhouse gases and none

of the air pollutants that create smog and cause health problems. If pure hydrogen is used as a fuel, fuel cells emit only heat and water as a byproduct.

A single fuel cell consists of an electrolyte and two catalyst-coated electrodes (a porous anode and cathode). While there are different fuel cell types as shown in Figure 2, all work on the same principle[11]:

- Hydrogen, or a hydrogen-rich fuel, is fed to the anode where a catalyst separates hydrogen's negatively charged electrons from positively charged ions (protons).
- At the cathode, oxygen combines with electrons and, in some cases, with species such as protons or water, resulting in water or hydroxide ions, respectively.
- For polymer electrolyte membrane and phosphoric acid fuel cells, protons move through the electrolyte to the cathode to combine with oxygen and electrons, producing water and heat.
- For alkaline, molten carbonate, and solid oxide fuel cells, negative ions travel through the electrolyte to the anode where they combine with hydrogen to generate water and electrons.
- The electrons from the anode side of the cell cannot pass through the electrolyte to the positively charged cathode; they must travel around it via an electrical circuit to reach the other side of the cell. This movement of electrons is an electrical current.

In most fuel cells, electrochemical oxidation of hydrogen takes place at the anode. In high-temperature fuel cells, it is possible to convert the fuel to hydrogen inside the cell by utilizing the heat from the electrochemical reaction, but otherwise it is necessary to

convert the primary fuel outside the stack into a hydrogen-rich gas that is fed to the anode. The coupling of fuel processing with the fuel cell operation is essential to achieve high plant efficiency. It is necessary to integrate the fuel processing system and the fuel cell stack to use the waster heat generated in the fuel cell stack itself. The aim is to reduce the amount of heat generated in the fuel cell power plant, because this can be transferred into electricity only via the Carnot cycle[12].

The primary objective of this chapter is to discuss the key role of free and supported oxide nanomaterials in clean hydrogen production and in the fabrication of fuel cells. Clean hydrogen production from the water-gas-shift (WGS) reaction will be discussed in detail in the second part of this chapter. As an example, we will show recent *in-situ* XRD and XAFS studies for the WGS on ceria-based nanocatalysts. Potential applications of oxide nanomaterials in fuel cells will be covered in the third part of this chapter, making emphasis on proton-exchange membrane fuel cells (PEMFCs) and solid oxide fuel cells (SOFCs).

II. H_2 Production

II.1 Oxide-based nanocatalysts and the water-gas-shift reaction

As it was mentioned above, hydrogen is manufactured primarily by the steam reforming process today: $C_nH_m + nH_2O \rightarrow nCO + (n-m/2)H_2$. The reformed fuel contains 1-10% CO, which degrades the performance of the Pt electrode in fuel cell systems.[13] In order to get clean hydrogen for fuel cells and other industrial applications, the water gas shift (WGS) reaction ($CO + H_2O \rightarrow CO_2 + H_2$) and preferential CO oxidation ($2CO + O_2 \rightarrow 2CO_2$) processes are critical (Figure 1)[10,14]. To accelerate them, heterogeneous

catalysts are frequently used.[15] A fundamental understanding of the configuration and properties of the active sites for the WGS reaction is a pre-requisite for designing catalysts with a high activity or efficiency.[15]

In industrial applications, the classical catalyst formulations contain a mixture of Fe and Cr oxides or Cu and Zn oxides.[15] There has been a lot of controversy about what is the active phase and the mechanism of the WGS reaction on these catalysts.[16] Most of the debate resides in the mechanistic area on whether the mechanism is *associative* taking place through intermediates such as formates or *regenerative* via redox reactions involving special forms of copper. In addition to formates, other species such as carbonates and hydroxycarbonates may be participating in the reaction.[15,16] A generally accepted mechanism for the WGS reaction yet fails to exist, and this is not surprising considering the complex nature of the catalyst surface. The need for *in-situ* characterization under reaction conditions is clear for these systems.[16]

The design of new WGS catalysts is aimed at obtaining systems with a high activity and a lower temperature of operation.[17] At the same time, one has to find a compromise between activity and cost. CeO_2-based nanocatalysts have been reported to be very promising for the WGS reaction. Among these materials, the two most studied systems currently are Cu- and Pt-based catalysts[16,17,18,19]. It is anticipated that, with proper development, metal promoted ceria catalysts should realize much higher CO conversions than even commercial CuZnO catalysts[20]. However, the roles played by ceria and the metal in the WGS reaction are still a matter of debate. The redox properties and oxygen storage capacity of ceria are usually considered important, while the metal plays a direct role in the mechanism of the WGS reaction.

A. WGS reaction on Cu-ceria nanocatalysts

Two synchrotron-based techniques, time-resolved X-ray diffraction (XRD) and X-ray absorption fine structure (XAFS), have been used for examining the behavior of Cu-ceria nanocatalysts *in situ* under the WGS reaction. The properties of $Ce_{1-x}Cu_xO_2$ catalysts prepared by a novel microemulsion method [21,22,23,24] can be compared to those of conventional CuO_x/CeO_2 and AuO_x/CeO_2 catalysts prepared by incipient impregnation methods.[25,26,27,28] The Cu atoms embedded in ceria have an oxidation state higher than those of the cations in Cu_2O or CuO.[29] The lattice of the $Ce_{1-x}Cu_xO_2$ systems still adopts a fluorite-type structure, but is highly distorted with multiple cation-oxygen distances in contrast to the single cation-oxygen bond distance seen in pure ceria. The doping of CeO_2 with copper introduces a large strain into the oxide lattice and favors the formation of O vacancies. Cu approaches the planar geometry characteristic of Cu(II) oxides but with a strongly perturbed local order. The chemical activities of the $Ce_{1-x}Cu_xO_2$ nanoparticles were tested using the reactions with H_2 and O_2 as probes.[29] During the reduction in hydrogen, an induction time was observed and became shorter after raising the reaction temperature. The fraction of copper that can be reduced in the $Ce_{1-x}Cu_xO_2$ oxides also depends strongly on the reaction temperature. A comparison with data for the reduction of pure copper oxides indicates that the copper embedded in ceria is much more difficult to reduce. The reduction of the $Ce_{1-x}Cu_xO_2$ nanoparticles is rather reversible and no significant amounts of CuO or Cu_2O phases are generated during reoxidation.[29] This reversible process demonstrates the unusual structural and chemical properties of the Cu-doped ceria materials. The chemical properties of these unusual materials were tested for the hydrogen production via the water gas shift reaction.

A typical set of time-resolved X-ray diffraction patterns is shown in Fig. 3a for a $Ce_{0.95}Cu_{0.05}O_2$ catalyst during the WGS reaction at different temperatures. Only the diffraction lines for ceria are seen[30,31], indicating that most of the copper is embedded in the host oxide forming a solid solution. In Figure 3b one can see a big increase in catalytic activity for the production of H_2 when going from 200 to 300 ^oC and then to 400 ^oC. CO_2 production followed the same curve as H_2 production and is not presented in Fig.3b. This turn-on of the catalytic activity did not produce diffraction lines for CuO_x or Cu species. As we will see in Figure 4 the Cu in $Ce_{0.95}Cu_{0.05}O_2$ is fully reduced under WGS conditions, but it is dispersed within the oxide probably forming nanoparticles that have sizes under 2 nm and do not yield diffraction peaks.

Similar experiments were carried out with *in situ* time-resolved XAFS. Figure 4a displays Cu K-edge XANES spectra collected over the $Ce_{0.95}Cu_{0.05}O_2$ catalyst cooled down to room temperature after the WGS reaction at 25, 100, 200, 300 and 400 ^oC. The corresponding Fourier transforms for the EXAFS region are shown in Figure 4b. The XANES data for temperatures above 200 ^oC, when substantial WGS activity was seen, show a line-shape typical of pure metallic copper[32,33]. In the Fourier transform for the EXAFS, the position of the main peak located between 1.1 and 2.0 Å at room temperature is similar to the first Cu–O coordination shell in CuO [34,35]. The Cu-O peak disappeared at high temperatures with a simultaneous increase of the Cu-Cu peak for metallic copper. The product curves from the *in situ* XAFS experiments are not shown here since they were similar to those for the *in situ* TR-XRD experiments. These results demonstrate the important role of metallic copper in the WGS reaction. Another set of experiments for a $Ce_{0.8}Cu_{0.2}O_2$ catalyst, Cu K-edge XANES spectra in the top panel of

Figure 5, also indicates that Cu is fully reduced when the catalyst displays high WGS activity.

Figure 5b compares the Ce L_3-edge XANES spectra from the $Ce_{0.8}Cu_{0.2}O_2$ sample in the water gas shift reaction at different temperatures with the spectrum for a $Ce(NO_3)_3 \cdot 6H_2O$ reference, in which the cerium atoms are trivalent. The two main peaks in the spectrum of the sample at room temperature are separated by approximately 7eV, in agreement with previous results[36]. Based on the comparison of the intensities of the spectra near the Ce^{3+} position, it is clear that oxygen vacancies and Ce^{3+} were formed during the WGS reaction. The amount of oxygen vacancies and Ce^{3+} is seen to increase with the raise of reaction temperature up to 300°C, but decreases at higher temperatures, especially above 400°C. When the $Ce_{0.8}Cu_{0.2}O_2$ catalyst was exposed to 5% CO in He, the amount of Ce^{3+} formed was bigger than for the experiments in Figure 5b and increased continuously with the temperature of exposure. These results show that ceria was oxidized by H_2O under the WGS reaction, with oxygen vacancies and Ce^{3+} being eliminated, especially at high temperature.[37,38]

Since Ce^{3+} is bigger than Ce^{4+}, a simple reduction leads to a ceria lattice cell expansion. Changes in the ceria lattice parameter can be directly related to the concentration of oxygen vacancies and Ce^{3+} cations in this oxide.[39,40,41] Figure 6a shows the lattice parameters for ceria determined from (111) diffraction peaks of TR-XRD patterns for $Cu_{0.2}Ce_{0.8}O_2$ under different gases at 400°C. The sample was first heated to 400°C in He. The ceria lattice displayed a significant increase after exposure to CO and a decrease in H_2O, indicating that CO reduced ceria while H_2O oxidized it. In other words, CO created oxygen vacancies while H_2O eliminated them.

In the bottom panel of Figure 6 are summarized the results of gas-switch experiments for $Cu_{0.2}Ce_{0.8}O_2$ at different temperatures. The ceria lattice parameter under the WGS reaction reflects a combination of the effects of CO reduction and H_2O oxidation, implying that oxygen vacancies on the fluorite phase are involved in the chemistry of the process.

The activity and behavior of ceria impregnated with copper oxides, CuO_x/CeO_2, during the WGS reaction has also been investigated.[29] Figure 7 compares the X-ray diffraction patterns for the $Ce_{1-x}Cu_xO_2$ and CuO_x/CeO_2 systems. The mixed-metal oxides exhibit only the diffraction lines of ceria since they are essentially solid solutions. On the other hand, diffraction peaks for CuO and Cu_2O are observed for the CuO_x/CeO_2 catalysts. In experiments of time-resolved XRD, it was found that the diffraction lines for CuO and Cu_2O disappeared under the WGS reaction, while diffraction lines for Cu appeared.[29] This $CuO_x \rightarrow$ Cu transformation is also clear in the Cu K-edge XANES spectra in Figure 8. The $5\%CuO_x/CeO_2$ catalyst initially exhibits the spectrum typical of CuO, but the line-shape of metallic Cu was observed at temperatures above 200 ^oC when the production of H_2 and CO_2 was significant. This trend corroborates that Cu, and no CuO_x, is the species present in the active sites for the WGS reaction.

Ce L_3-edge XANES spectra (not shown) demonstrated the partial reduction of ceria in $5\%CuO_x/CeO_2$ during the WGS, but the formation of Ce^{3+} was not as pronounced as seen in Figure 5b for $Cu_{0.2}Ce_{0.8}O_2$, probably because the copper in the impregnated sample had a lower dispersion within the oxide support than in the doped sample. Figure 9 summarizes the behavior of the ceria lattice in $5\%CuO_x/CeO_2$ under different gases at 400 ^oC. Exposure to CO produces the formation of Ce^{3+} and expands

the ceria lattice. The adsorption of H_2O on the O vacancies removes the Ce^{3+} and contracts the lattice. These are in agreement with those changes for the doped samples shown in Fig. 4a.

B. WGS reaction on Au-ceria nanocatalysts

During the past decade, many studies have established that Au on reducible oxides has a remarkable catalytic activity for many important industrial reactions, including the low-temperature oxidation of CO, the water gas shift reaction, hydrocarbon oxidation, NO reduction and the selective oxidation of propylene to propylene oxide.[42,43,44,45,46,47] Au-CeO_2 nanocatalysts have recently been reported to be very promising catalysts for the WGS reaction.[44,47] As prepared, these catalysts contain nanoparticles of pure gold and gold oxides (AuO_x) dispersed on a nano ceria support. The ceria support may not be a simple spectator in these systems.[48] Pure ceria is a very poor WGS catalyst, but the properties of this oxide were found to be crucial for the observed activity of the Au-CeO_2 catalysts.[43,49]

Several models have been proposed for explaining the unusual catalytic properties of gold supported on oxides:[41,42,45] From special chemical properties resulting from the limited size of the active gold particles (usually less than 5 nm), to the effects of metal:support interactions. In particular, it has been suggested by several authors that the active phase in Au-CeO_2 catalysts are AuO_x nanoparticles or more specifically cationic $Au^{\delta+}$ species.[44,50] Similar $Au^{\delta+}$ centers have been proposed as the active centers for the oxidation of CO on Au/MgO catalysts.[51] In contrast, Haruta and co-workers have indicated that the active species are small metallic gold particles.[43,46] In studies dealing

with a $Au/TiO_2(110)$ model catalyst, Goodman et al found that for catalytic activity metallic gold is indispensable.[45,52,53] However, the catalytic activity could be further enhanced by perturbing the electronic structure of gold ($Au^{\delta-}$) by a strong interaction between the metal and O vacancies in the oxide support.[42,43,46,53,54,55] In principle, the active sites for the catalytic reactions could be located only on the supported Au particles or on the perimeter of the gold-oxide interface.[42,46,54,55,56,57]

In order to address these issues, an *in situ* time-resolved characterization of the $Au\text{-}CeO_2$ catalysts under operational conditions is critical. Synchrotron-based *in situ* time-resolved X-ray absorption spectroscopy[47,58] and time-resolved X-ray diffraction[59,60] were employed to study the WGS reaction over nanostructured $Au\text{-}CeO_2$ catalysts. In addition, the oxidation and reduction of Au nanoparticles supported on a rough ceria film or a $CeO_2(111)$ single crystal were investigated using photoemission.[47,48]

We will begin by examining results of *in situ* TR-XRD experiments for the WGS reaction over a 2.4wt%Au-Ce(10at%Gd)O_x catalyst.[47] A typical set of results is shown in Figure 10. The catalyst was held at temperatures of 300, 400 and 500 ^oC. The X-ray diffraction pattern for the as prepared catalyst, bottom of Figure 10, showed the typical peaks for nanoceria[47] and no features that could be attributed to nanoparticles of Au or AuO_x. The gold species were present as aggregates or clusters that had sizes below 2 nm. Exposure of the $Au\text{-}CeO_2$ catalyst to a mixture of CO/H_2O at temperatures of 300-500 ^oC led to the formation of H_2 and CO_2 without inducing the appearance of diffraction peaks for AuO_x or Au species. The catalytically active gold particles had a very small size (< 2 nm) and were in close contact with the ceria support since they did not agglomerate at temperatures as high as 500 ^oC.

The chemical state of gold during the WGS was determined by means of *in situ* XANES. Figure 11 shows Au L_3-edge XANES spectra collected at room temperature for fresh catalysts with a Au content of 0.5wt% (dashed trace) or 2.4wt% (solid traces).[47] The line shape of these two spectra is very similar and shows a clear feature at ~ 2.5 eV above the edge that is not seen for metallic gold and is characteristic of gold oxides.[61] The intensity of this peak is higher than that observed for Au_2O and closer to that seen in Au_2O_3.[61] Once the 2.4wt%Au-Ce(10at%Gd)O_x catalyst was exposed to a mixture of CO/H_2O at elevated temperatures, the XANES features for gold oxide disappeared. At temperatures above 200 ^oC, when significant WGS activity was detected, the line-shape of the Au L_3 edge resembled that of pure gold.[47] The XANES spectra in Figure 11 were obtained under a reaction mixture of 5%CO and 3% H_2O in He (total flow ~ 10 ml/min). Similar results were found when using a 1% CO and 3% H_2O in He reaction mixture.[47] The AuO_x in the Au-CeO_2 catalysts was also fully reduced upon exposure to CO or H_2 at 200-500 ^oC. The *in situ* TR-XANES data indicate that cationic $Au^{\delta+}$ species *cannot be* the key sites responsible for the WGS activity in Figure 10, since they do not exist under reaction conditions. Small Au aggregates (< 2 nm in size) supported on ceria exhibit a WGS activity not seen for pure gold or ceria.

In a separate set of experiments, the interaction of O_2 and mixtures of CO/H_2O with gold nanoparticles supported on a well-defined CeO_2(111) surface or rough ceria films was investigated. These experiments were done using a ultra-high vacuum (UHV) chamber that has attached a high-pressure cell or batch reactor.[48,62,63,64] The sample could be transferred between the reactor and vacuum chamber without exposure to air. Small coverages of gold (0-0.2 monolayer) were vapor-deposited on the CeO_2(111) surface at

25 ^{o}C. At these coverages the admetal grows forming three-dimensional (3D) islands on the CeO_2(111) substrate which have sizes in the range of 0.5- 3 nm.[47] The Au/CeO_2(111) surfaces were exposed in the batch reactor to a mixture of H_2O (10 Torr) and CO (pressures varying from 2 to 20 Torr) at temperatures of 300-400 ^{o}C. The production of H_2 and CO_2 through the WGS was observed. After pumping the gases, photoemission spectra (Au 4f and Ce 3d core-levels) indicated that Au remained in a zero-valent state (i.e. no formation of AuO_x) and there was a partial reduction of the CeO_2(111) support.

Interfaces of AuO_x/CeO_2 were prepared by first vapor-depositing small amounts of Au (< 0.2 ML) on a Ce film supported on Pt(111).[64] The Au-Ce/Pt(111) systems were then oxidized by reaction with 500 Torr of O_2 in a high-pressure cell. This produced AuO_x/CeO_2 interfaces that have the typical Ce 3d features of ceria[47,65] and Au $4f_{7/2}$ peaks located in between those expected for Au^{+1} and Au^{+3}.[47] As in the case of Au/CeO_2(111), the AuO_x/CeO_2 interfaces were exposed to mixtures of CO/H_2O at 300-400 ^{o}C in a reaction cell. Figure 12 displays typical results of photoemission. Initially, Au^{3+} and some Au^{0} were present in the AuO_x/CeO_2 system. Exposure to a mixture of 5 Torr of CO and 10 Torr of H_2O at 300 ^{o}C led to a full reduction of the gold oxide and partial reduction of ceria (Ce 3d spectrum, not shown). The gold oxide in the AuO_x/CeO_2 interfaces was fully reduced upon exposure to CO, H_2 or reaction mixtures that had a CO/H_2O ratio varying from 0.2 to 2.[47]

The top panel in Figure 13 compares the WGS activity of Au/CeO_{2-x}(111) and Au/CeO_{2-x} catalysts that contained the same amount of gold (~ 0.15 monolayer). These catalysts were pre-conditioned by exposing the fresh Au/CeO_2(111) and AuO_x/CeO_2 systems to a mixture of 20 Torr of CO and 10 Torr of H_2O for 5 minutes at 350 ^{o}C.

Photoemission indicated that the catalysts contained only pure Au and a quantitative analysis of the line-shape of the Ce 3d core levels [66] gave stoichiometries of $Au/CeO_{1.94}(111)$ and $Au/CeO_{1.88}$. These compositions remained essentially constant during the experiments in the top panel of Figure 13. In these experiments, the $Au/CeO_{1.94}(111)$ and $Au/CeO_{1.88}$ catalysts were under a mixture of 20 Torr of CO and 10 Torr of H_2O for 5 minutes at 350 ^oC. Then, the amount of H_2 and CO_2 produced through the WGS was measured. Both catalysts have a much higher activity than that observed for Cu(110) and Cu/ZnO catalysts under similar reaction conditions.[67] The catalyst generated from AuO_x/CeO_2 was clearly the more active, probably because it contained a larger amount of surface defects and O vacancies than the catalyst generated from $Au/CeO_2(111)$.[47]

The bottom panel in Figure 13 shows the effect of Au coverage on the catalytic activity of $Au/CeO_{2-x}(111)$. These surfaces were pre-conditioned as described above, and then we measured the catalytically produced H_2 and CO_2 after exposure to a mixture of 20 Torr of CO and 10 Torr of H_2O for 5 minutes at 350 ^oC. A maximum in the catalytic activity is seen for Au coverages of 0.4-0.5 ML. The drop in the catalytic activity at high Au coverage is probably an effect of a growth of the Au nanoparticles (> 3 nm in size),[47,68] and agrees with the fact that there is no increase in WGS activity when going from a 2.4%wtAu- to a 5.0%wtAu-Ce(10at%Gd)O_x catalyst.[44]

The results of photoemission and *in situ* TR-XAS indicate that the active phase of the gold/ceria catalysts for the WGS contained pure Au and CeO_{2-x}. This is consistent with studies which show that Au as an admetal facilitates the reduction of ceria.[69] The generation of Ce^{3+} in ceria produces an expansion in the unit cell of the oxide that can be

monitored with TR-XRD.[47] Figure 14 shows the lattice parameters for ceria determined from (111) diffraction peaks of TR-XRD patterns for 2.4wt%Au-Ce(10at%Gd)O_x under different gases at 500^{o}C. The sample was first heated from 25 to 500^{o}C in He, producing an increase of ~ 0.02 Å in the ceria lattice due to thermal expansion.[47] The oxide lattice varied significantly after exposure to CO, ~ 0.04 Å increase as a consequence of the formation of O vacancies and Ce^{3+}, or H_2O, ~ 0.03 Å decrease probably as a result of the decomposition of this adsorbate on the O vacancies. Under a mixture of CO/H_2O, O vacancies were formed that could be removed only upon exposure to O_2. The changes of ceria in Au-CeO_x catalysts were consistent with those changes observed for ceria in Cu-CeO_x catalysts during similar gas switch experiments, indicating the same role played by ceria for both systems.

From the data in Figures 11-14, it appears that the rate determining steps for the WGS at temperatures above 250 ^{o}C occur at the gold-ceria interface, with the active phase involving small gold clusters (< 2 nm) and O vacancies. A strong interaction between the admetal and support prevents the generation of big particles (> 2 nm) of gold and is probably a key issue for determining the catalytic properties of the gold/ceria system. It is not necessary to invoke a special catalytic activity for nonmetallic gold nanoparticles (AuO_x).[47]

Figure 15 compares the conversion of CO during the WGS reaction over the same amount (~5mg) of 2.4%AuO_x/CeO_2, 5%CuO_x/CeO_2, $Ce_{0.8}Cu_{0.2}O_2$, $Ce_{0.95}Cu_{0.05}O_2$ and CuO at 400 ^{o}C. No activity was observed over pure nano ceria under the present operating conditions. The 2.4%AuO_x/CeO_2, 5%CuO_x/CeO_2 and $Ce_{0.95}Cu_{0.05}O_2$ catalysts have a similar activity. Figure 15 clearly shows that the catalyst based on pure CuO has

little activity. This catalyst certainly had the largest concentration of copper sites among the studied samples. These results indicate that interactions between copper and ceria enhance the activity of the metal in Cu-CeO_2 catalysts, suggesting that the WGS reaction may take place preferentially on the metal/ceria interface. The same may be valid also for the Au-CeO_2 catalyst since this system is more active than either pure gold or pure ceria.[47] The moderate activity of the $Ce_{0.8}Cu_{0.2}O_2$ catalyst may be a consequence of the formation of a large amount of strongly bound carbonates on its surface.[29] The CuO_x and AuO_x species present in the fresh Cu-CeO_2 and Au-CeO_2 nanocatalysts of Figure 15 do not survive above 200°C under the WGS conditions.[29,47] Data of time-resolved XRD and XANES indicate that metallic copper or gold and oxygen vacancies in ceria are involved in the generation of the catalytically active sites.

C. WGS on other oxide-based catalysts

There has been an interest in the Pt/CeO_2 system since the early 1980s, when in connection with the development of the three-way catalysts for reducing exhaust engine pollution it was discovered that such system enhances the rate of the WGS.[70] Academic research on Pt, Pd, Rh, Ni, Fe, and Co-ceria as catalysts for the WGS involved mechanistic studies and the effect of the ceria oxygen-storage properties on the WGS activity.[71,72] The performance of the catalysts was strongly affected by the method used for the pre-treatment of the ceria support.[71] It was proposed that the WGS occurred primarily through a bifunctional mechanism in which CO adsorbed on the precious metal is oxidized by ceria, which in turn is oxidized by water.[71,72] A reaction mechanism that involves a surface formate intermediate cannot be ruled out.[73] Enhancement of the WGS

activity of Pt/CeO_2 has been observed after doping of the oxide with Zr.[74] The doping with zirconia decreases the temperature for the surface reduction step in the WGS process.[74] Pt/MgO and Pt/ZrO_2 are active catalysts for the WGS reaction,[73] but they are not as good as Pt/CeO_2.

Ruthenium deposited on α-Fe_2O_3 has been mentioned in the literature as giving promising WGS conversions.[75] Non-precious metal formulations for the WGS are sought because of their low cost. The WGS activity of alkaline-promoted basic oxides based on Mg, Al, La, Nd, Pr, Mn and Mg has been tested and found satisfactory at elevated temperatures (> 400 C).[76] Mixtures of Co- or Ni- promoted Mo, V, or W oxides are also catalytically active under similar conditions.[76]

II.2 Production of H_2 through other methods

Hydrogen can be produced by the steam reforming, $C_nH_m + nH_2O \rightarrow nCO + (n-m/2)H_2$, or the partial oxidation, $C_nH_m + n/2\ O_2 \rightarrow nCO + (m/2)H_2$, of hydrocarbons. Natural gas is the major feedstock for the production of hydrogen via syngas.[77] Because CH_4 is a very stable molecule it has to be processed under very severe conditions.[77] The steam reforming of methane is a highly endothermic reaction (ΔH^o= 206 kJ/mol), whereas the partial oxidation is slightly exothermic (ΔH^o= -36 kJ/mol). The traditional methane steam reforming catalysts for the production of hydrogen and synthesis gas contain Ni/NiO or CoO_x supported on alumina[78] or combined with a rare-earth oxide like ceria.[79] The catalysts are frequently promoted with alkali and alkali-earth oxides to improve their stability and facilitate coke gasification.[78]

Partial oxidation of methane is a much faster reaction than steam reforming, offering therefore the advantage of smaller reactors and higher throughputs.[80] Catalysts include mixtures of NiO-MgO, nickel modified hexa-aluminates and platinum group metals deposited on alumina or ceria-containing supports.[80,81,82] Examples of catalysts for the oxidative reforming of methane based on ceria are: Ni/CeO_2 and Ni/CeO_2-ZrO_2,[83] Pt/CeO_2-ZrO_2,[82,84] and Ru/CeO_2-ZrO_2.[82] The activity of these catalysts seems to be enhanced by metal-support interactions and the oxygen storage capacity (OSC) of ceria under oxidizing-reducing conditions.[39,82,85] More systematic studies need to be done investigating the application of oxide nanocatalysts in the production of hydrogen through steam reforming or the partial oxidation of hydrocarbons.

Hydrogen can be obtained directly from methanol following three different processes: (i) steam reforming, (ii) decomposition, and (iii) partial oxidation.[77] Typical catalysts for methanol steam reforming are based on Cu-ZnO-Al_2O_3.[86] Sometimes zirconia is added to these catalysts to enhance its activity or to improve its selectivity towards carbon dioxide.[87] NiO and CuO_x supported on high surface area carriers, and promoted with other metal oxides, have been used for methanol decomposition: $CH_3OH \rightarrow CO + 2H_2$.[88] Small nanoparticles (3-8 nm) of copper oxide undergo partial reduction before becoming catalytically active for methanol decomposition.[89] Partial oxidation of methanol over Cu-containing catalysts produces mainly carbon dioxide and hydrogen: $CH_3OH + 0.5O_2 \rightarrow CO_2 + 2H_2$. Cu-ZnO-$Al_2O_3$ catalysts used for methanol synthesis display a very good performance in methanol partial oxidation.[77]

Another possible routes for the production of H_2 are thermochemical water splitting and photoassisted water splitting.[2,5,77] At the present time these processes are not

efficient enough for the industrial production of hydrogen. Photochemical water splitting to H_2 and O_2 has been successfully carried out using ultraviolet irradiation of aqueous suspensions (or thin-film photoanodes) of various photocatalysts including TiO_2,[90] transition-metal doped TiO_2,[91,92] $SrTiO_3$,[93] and transition-metal loaded $SrTiO_3$.[94] Among these photocatalysts, TiO_2 is the one most frequentely employed because of its low cost, nontoxicity, and structural stability.[92] However, pure titania is only activated by ultraviolet light.[90] Recently, N-doped titania ($TiO_{2-x}N_x$) has been synthesized and used as a photocatalyst that utilizes visible light (> 420 nm).[95,96,97] This material absorbs solar light in a region where TiO_2 or $SrTiO_3$ do not due to their wide band gaps. Such a behavior is very important for practical applications since solar light contains less than 5% of ultraviolet radiation. In principle, a dopant element can induce energy levels within the band gap of TiO_2 that may increase the yield for electron-hole pair formation under illumination with visible light.[90,91,95] Two different models have been proposed to explain the good performance of $TiO_{2-x}N_x$ as a photocatalyst.[95,98,99] In one model, hybridization of the N 2p states of the dopant with the O 2p valence band of TiO_2 leads to band narrowing.[95] Optical absorption studies on N-doped TiO_2 point to a gap narrowing,[95] but no band gap narrowing has been observed in photoemission studies.[100] In the second model, the dopant N 2p levels form localized states within the band gap just above the O 2p valence band maximum for titania.[98] For a detailed discussion of the photochemical properties of pure and doped nanoparticles of TiO_2, the reader is referred to chapter 16 in this book.

III. Fuel Cells

In this section we will describe two types of fuel cells that make use of the H_2 produced through the processes described in the previous section. These fuel cells have found a place in technological applications and they may use either H_2 or hydrogen-rich fuels in their operation. However, if pure hydrogen is used as a fuel, the fuel cells emit only heat and water as a byproduct.

III.A Polymer Electolyte Membrane Fuel Cell (PEMFC)

The PEMFC, more commonly known as the proton exchange membrane fuel cell, was first used in the 1960s as an auxiliary power source in the Gemini space flights. Advances in this technology were stagnant until the late 1980s when the fundamental design underwent significant reconfiguration. Nowadays, the PEMFC is one of the most promising fuel cell types for widespread use because it offers several advantages for transport and a number of other applications. Its low-temperature operation, high power density, fast start-up, system robustness, and low emissions have ensured that the majority of motor manufacturers are actively pursuing PEMFC research and development. Already in Europe with demonstration buses and passenger vehicles in California, for example, a first market introduction of fuel cell vehicles will be seen in the near future.[101]

As indicated in Figure 16, a single proton-exchange membrane (PEM) cell is comprised of three types of components: a membrane-electrode assembly (MEA), two bipolar plates, and two seals. In its simplest form, the MEA consists of a membrane, two dispersed catalyst layers, and two gas diffusion layers (GDL). The membrane separates the half reactions allowing protons to pass through to complete the overall reaction. The electron created on the anode side is forced to flow through an external circuit thereby

creating current. The GDL allows direct and uniform access of the fuel and oxidant to the catalyst layer, which stimulates each half reaction. In a fuel cell stack, the bipolar plates are vital components. Each bipolar plate supports two adjacent cells. The bipolar plates typically have four functions: (1) to distribute the fuel and oxidant within the cell, (2) to facilitate water management within the cell, (3) to separate the individual cells in the stack, and (4) to carry current away from the cell. In the absence of dedicated cooling plates, the bipolar plates also facilitate heat management. Different combinations of materials, fabrication techniques, and layout configurations have been developed for these plates to achieve high performance and optimal cost.[101]

Mehta and Cooper reviewed the material needs for designing and manufacturing PEM fuel cells for vehicle applications.[102] In their article, 16 polymer electrolyte membranes, 2 types of gas diffusion layers (GDL), 8 types of anode catalysts, 4 types of cathode catalysts and over 100 bipolar plate designs are recommended for further study. The prime requirements of fuel cell membranes are high proton conductivity, low methanol/water permeability, good mechanical and thermal stability and moderate price.[102] Membranes and their operating parameters have a profound influence on the performance of PEMFCs. Membranes built from perfluorinated ionomers, hydrocarbon and aromatic polymers and acid–base complexes have been described by Smitha et.al.[103] Membranes containing nanoarrays of NiO, TiO_2 and titanium silicates have prepared and tested.[104, 105] Promising avenues for further research in this area have been identified.[102,103,104,105]

Farrauto et. al. reviewed methods for the production of hydrogen for the PEM fuel cells.[106] Technologies including heterogeneous catalysts for the water gas shift

reaction, the reforming of methanol (either autothermal or steam reforming), the preferential oxidation of CO, and anode tail gas combustion were discussed in detail in this article.[106] The rapid development in recent years of the PEM fuel cell technology has stimulated research in all areas of fuel processor catalysts for hydrogen generation. The principal aim is to develop more active catalytic systems that allow for the reduction in size and increase the efficiency of fuel processors. The overall selectivity in generating a low CO content hydrogen stream as needed by the PEM fuel cell is dependent on the efficiency of the catalysts utilized in each segment of the fuel processor. The hydrogen produced via steam reforming and partial oxidation of hydrocarbons always contains CO.[76,77] As discussed in the previous section, oxide-based nanocatalysts can be very efficient for the removal of CO and the production of nearly pure H_2 through the water-gas shift reaction.

In a PEM fuel cell, the type of fuel used dictates the appropriate type of anode or cathode catalysts needed to facilitate the chemical transformations inside the cell. Within this topic, tolerance to carbon monoxide is an important issue. The amount of CO present in the feed can be greatly reduced through the water-gas shift, but CO always will be present at the ppm level. It has been determined that the PEM fuel cell must be capable of tolerating a CO concentration of at least 100ppm in order to reduce the size of the hydrogen production/cleaner unit[107] An approach is to alloy the anode catalyst to minimize its sensitivity towards CO; one (a binary catalyst) or sometimes two elements (a ternary catalyst) are added to the base catalyst, usually Pt/C. Mehta and Cooper summarized over 26 different kinds of catalysts for the MEA component of PEM fuel cells.[102] The anode catalysts were divided into three groups based on the number of

metal elements used: single metal catalyst (Pt/C), binary catalysts (Pt-Ru/C, Pt-Mo/C, Au-Pd/C, etc) and tertiary catalysts (Pt-Ru-Mo/C, Pt-Ru-W, Pt-Ru-Al_4, and Pt-Re-(MgH_2), etc.).[102] In addition to Pt/C, Pt-Ni/C and Pt-Co/C were reported for cathode applications.[108] Anode and cathode catalysts built from oxide nanostructures that have a reasonable high conductivity and resistance to CO are also under consideration and being tested.[104,105]

The design of electrodes for PEMFCs is a delicate balancing of transport media.[109] Conductance of gas, electrons, and protons must be optimized to provide efficient transport to and from the electrochemical reactions. This is accomplished through careful consideration of the volume of conducting media required by each phase and the distribution of the respective conducting network.[109] In addition, the issue of electrode flooding cannot be neglected in the electrode design process. New fabrication methods, which have now become conventional, were adopted and optimized to a high degree. Possibly, the most significant barrier that PEM fuel cells have to overcome is the costly amount of platinum required as a catalyst. The large amount of platinum in the original PEM fuel cells was one of the reasons why fuel cells were excluded from commercialization.[102,109] Thus, the reconfiguration of the PEM fuel cell was targeted rather directly on the electrodes employed and, more specifically, on reducing the amount of platinum in the electrodes. This continues to be a driving force for further research on PEM fuel cell electrodes[109] and low cost conducting oxide nanoarrays could be an alternative.[104,105]

III.B Solid oxide fuel cell (SOFC)

The solid oxide fuel cell is an all-solid device that converts the chemical energy of gaseous fuels such as hydrogen and natural gas to electricity through electrochemical processes.[110,111] These fuel cells provide many advantages over traditional energy conversion systems including high efficiency, reliability, modularity, fuel adaptability, and very low levels of NO_x and SO_x emissions. The efficiency of SOFCs is inherently high as it is not limited by the Carnot cycle of a heat engine.[110] A solid oxide fuel cell essentially consists of two porous electrodes separated by a dense, oxygen ion conducting electrolyte.[110,111] They can be arranged in a planar or tubular configuration (Figure 17).[111] The cathode or air electrode operates at elevated temperatures (usually 800-1100 C) and participates in the oxygen reduction reaction:

$$0.5O_2(g) + 2e \rightarrow O^{2-}(s)$$

i.e. oxygen in the gas phase is reduced to oxide ions, consuming two electrons in the process. The air electrode frequently consist of lanthanum manganite doped with alkaline and rare earth elements.[111,112] Lanthanum manganite ($LaMnO_3$) is a p-type perovskite oxide and shows reversible oxidation-reduction behavior. Recently, a composite cathode was fabricated using well-dispersed nano-size grains of $La(Sr)MnO_3$ and Y_2O_3 stabilized ZrO_2.[113] The composite cathode had a unique morphology that led to high electrochemical activity at 800 C, suggesting that intermediate temperatures (< 800 C) of operation can be achieved by using composite arrays of oxide nanoparticles.[113]

SOFCs are based on the concept of an oxygen ion conducting electrolyte through which the oxide ions (O^{2-}) migrate from the air electrode (cathode) side to the fuel electrode (anode) side where they react with the fuel (H_2, CH_4, etc) to generate an electrical voltage. Fluorite-structured oxide materials such as yttria stabilized zirconia

(YSZ), rare earth doped ceria, and rare earth doped bismuth oxide are widely used for electrolytes in SOFCs.[111,112] The oxygen-ion conducting capabilities of these oxides in many cases improve when going from the bulk to the nanoscale (see chapter 13 in this book), also improving their performance in SOFCs.[105,110,113,114]

In a SOFC, the anode is the electrode for the electrochemical oxidation of the fuel. Hydrogen oxidation is one of the most important electrode reactions in SOFCs. The process for the electrochemical oxidation of H_2 can be written as

$$H_2(g) + O^{2-}_{oxide} \rightarrow H_2O(g) + 2e$$

where O^{2-}_{oxide} is an oxygen ion in the electrode. To minimize the polarization losses of the H_2 oxidation reaction, anode materials should have a high electronic conductivity and electrocatalytic activity.[110,114] Nanostructured oxides can be particularly useful in this respect.[105,113] Current activities in the area of materials development for SOFCs are increasingly focused on decreasing the operating temperatures of the cell from 1000-1100C to 500-800 C.[111,112,113] The most common anodes for SOFCs contain a metal-oxide cermet: Ni/Y_2O_3-ZrO_2 (the so-called Ni/YSZ cermet).[111,114] Conventional Ni/YSZ cermet anodes are usually made of commercial NiO and YSZ powders, which are then homogenized by mechanical mixing and milling. The NiO/YSZ ink is applied to the YSZ electrolyte and sintered to form a porous Ni/YSZ cermet electrode.[111] The performance of these cermet anodes depends critically on the microstructure and distribution of the Ni and YSZ phases.[111] The use of nano-size grains for the oxide precursors leads to a better dispersion/mixing and a subsequent improvement in the performance of the Ni/YSZ cermets.[113,114] The Ni/YSZ cermets have very good electrocatalytic properties for cells that use H_2 as a fuel, but suffer a series of drawbacks in systems where natural gas is the

fuel, notably the sulfur poisoning and carbon deposition caused by the cracking of C2 and higher hydro-carbons.[114] Theoretical studies of more conventional supported nickel catalysts have focused on ensemble size effects, nickel crystallite size effects, and control of highly active step and edge sites to reduce carbon formation[115]. The acidity of the support has also been considered important, with acidic supports such as Al_2O_3 to be avoided, and basic supports such as MgO or $MgAl_2O_4$ being preferred[116]. With these latter supports, it is believed that adsorption of H_2O is increased, facilitating the gasification of carbon that is deposited on the surface[117]. Takeguchi et al investigated the carbon deposition during the steam reforming of methane on Ni/YSZ anodes modified with the addition of MgO, CaO, SrO or CeO_2 .[118,119] The presence of nanoparticles of CaO, SrO and CeO_2 suppressed the carbon deposition while the addition of MgO nanoparticles promoted it and decreased the steam reforming activity of the anodes. A high content (1-2 wt%) of CeO_2 and SrO in the Ni/YSZ cermets also led to a substantial decrease in the steam reforming activity. However, other literature showed that MgO has unique properties in its interaction with NiO, due to its ability to form a solid solution. On reduction, Ni appears to be stabilized relative to sintering and carbon formation, as it maintains a strong interaction with the MgO or a MgO-NiO solid solution[116]. Sample preparation methods and catalyst compositions played important roles in the different behaviors of the MgO containing system and need to be investigated more thoroughly in the future.[116] Additional studies showed that the addition of Ru and Pt promotes the reforming activity and suppresses the carbon deposition.[118,119]

Several studies have been carried out on the use of electronic or mixed conducting oxides to make alternative metal/oxide cermets such as ceria stabilized zirconia (CeO_2-

ZrO_2), calcium-doped ceria (Ca-CeO_2), yttria-doped ceria (YDC), samaria-doped ceria (SDC), and praseodymium oxide (PrO_x).[114] Mixed results were reported, and the performance of the electrode depends strongly on the preparation method.[114] Eguchi et al observed that the activity of Ni/oxide cermets for hydrogen oxidation increased following the sequence:[120]

$$Ni/YSZ < Ni/CeO_x < Ni/SDC < Ni/PrO_x$$

The improved performance was attributed to the increase of the effective reaction area due to the ionic conduction of the oxides.[117] A comparison of the hydrogen-oxidation activity of Ni/CeO_2 cermets prepared with bulk NiO and CeO_2 or with nano NiO (3-6 nm) and CeO_2 (5-8 nm) shows that the second type of electrode is ~ 4 times more active than the first.[121]

Gorte and co-workers focused their efforts on the development of Cu/CeO_2/YSZ based anodes.[114,122,123,124] Copper is much less reactive than nickel. Copper is inert to hydrogen or hydrocarbon oxidation and has no catalytic activity for the formation of C-C bonds, thus suppressing the carbon deposition. The primary function of copper in the cermet anodes is to provide a path for the conduction of electrons.[120,121] A pure Cu/YSZ anode has very low electrochemical activity for both H_2 and CH_4 oxidation reactions. Ceria catalyst was added to the Cu/YSZ cermet to improve the electrode activity.[119,120]

Pure or doped titanates (TiO_2, $SrTiO_3$, $ZrTiO_4$) and lanthanum chromites ($LaCrO_3$) have been tested as anode materials.[110,114] Chromite/titanate based perovskite anodes generally show much poorer electrochemical activity for H_2 oxidation as compared to that of Ni/YSZ cermet anodes despite of the high electrical conductivity of some of the perovskites.[114] The performance of these oxides can be improved when going

from the bulk to the nano scale,[105,118] but then there are issues with their long term stability.[112] In general, they do not show clear advantages when combining activity and stability and comparing with respect to the properties of the Ni/YSZ system.

IV. Conclusions:

Oxide nanosystems play a key role as components of catalysts used for the production of H_2 via the steam reforming or the partial oxidation of hydrocarbons, and for the water-gas shift reaction. The behavior seen for Cu-ceria and Au-ceria WGS catalysts indicates that the oxide is much more than a simple support. The special chemical properties of the oxide nanoparticles (defect rich, high mobility of oxygen) favor interactions with the reactants or other catalyst components. More *in-situ* characterization and mechanistic studies are necessary for the optimization of these nanocatalysts.

The use of oxide nanomaterials for the fabrication of PEMFCs and SOFCs can lead to devices with a high practical impact. One objective is to build electrodes with low cost conducting oxide nanoarrays. The electron and oxygen-ion conducting capabilities of many oxides improve when going from the bulk to the nanoscale. Furthermore, one can get a more homogeneous surface morphology and an increase of the effective reaction area. Much more fundamental and practical research needs to be done in this area.

Acknowledgement

The work done at Brookhaven National Laboratory was financed through contract DE-AC02-98CH10086 with the U.S. Department of Energy (DOE), Division of Chemical Sciences. The word done at Pacific Northwest National Laboratory operated by Battelle Memorial Institute was financed by the U.S. Department of Energy under Contract DE-AC05-76RL01830.

References:

[1] Information from R. E. Smalley, Rice University, talk at Brookhaven National Lab, Oct. 2004.

[2] A. Midilli, M. Ay, I. Dincer, M.A. Rosen , Renewable and sustainable energy reviews, 9(2005), 255-271.

[3] Energy Policy Act (EPAct), 1992.

[4] J.R. Rostrup-Nielsen, Catalysis Reviews, 46(3-4) (2004), 247.

[5] a) President's Hydrogen Initiative, 2003. b) M.Z. Jacobson, W.G. Colella, D.M. Golden, D. M., Science, 308 (2005) 1901.

[6] Energy Policy Act (EPAct), 1992.

[7] President's Hydrogen Initiative, 2003.

[8] M. Z. Jacobson, W. G. Colella and D. M.Golden, Science, 308 (2005), 1901.

[9] R. Farrauto, S. Hwang, L. Shore, W. Ruettinger, J. Lampert, T. Giroux, Y. Liu, O. Ilinich, Auu. Rev. Mater. Res. 33 (2003), 1.

[10] a) J.J. Spivey, Catal. Today, 100 (2005) 171. b) A.Y. Tonkovich, J.L. Zilka, M.J. LaMont, Y. Wang, R.S. Wegeng, Chem. Eng. Sci. 54 (1999), 2947.

[11] a) B. C. H. Steele and A. Heinzel, Nature, 414 (2001), 345. b)

http://www.eere.energy.gov/

[12] J.R. Rostrup-Nielsen, J. Sehested, and J.K. Nørskov, Adv. Catal. 47 (2002), 65

[13] a) Y. Liu, Q. Fu, M. Flytzani-Stephanopoulos, Catal. Today, 93-95 (2004) 241. b) D.J. Suh, C. Kwak, J.H. Kim, S.M. Kwon, T.J. Park, J. Power Sources, 142 (2005), 70.

[14] C. Song, Catal. Today, 77 (2002), 17.

[15] Y. Li, Q. Fu, M. Flytzani-Stephanopoulos, Appl. Catal. B, 27(2000), 179.

[16] C. Rhodes, G.J. Hutchings and A.M. Ward, Catal. Today 23 (1995), 43.

[17] N. A. Koryabkina, A. A. Phatak, W. F. Ruettinger, R. J.Farrauto and F. H. Ribeiro, J. Catal., 217 (2003), 233.

[18] Y. Liu, Q. Fu and M. F. Stephanopoulos, Catal. Today, 93-95 (2004), 241

[19] Q. Fu, H. Saltsburg, M. Flytzani-Stephanopoulos, Science, 301 (2003), 935.

[20] G. Jacobs, E. Chenu, P. M. Patterson, L. Williams, D. Sparks, G. Thomas and B. H. Davis, Appl. Catal. A: General 258 (2004), 203.

[21] M. Fernández-García, A. Martínez-Arias, A. Guerrero-Ruiz, J. C. Conesa and J. Soria, J. Catal. 211 (2002), 326.

[22] A. Iglesias-Juez, A. B. Hungría, O. Gálvez, M. Fernández-García, A. Martínez-Arias, A. Guerrero-Ruiz, J. C. Conesa and J. Soria, Stud. Surf. Sci. Catal., 138 (2001), 347.

[23] M. Fernández-García, A. Martínez-Arias, A. B. Hungría, A. Iglesias-Juez, J. C. Conesa and J. Soria, Phys. Chem. Chem. Phys. 4 (2002), 2473.

[24] A. B. Hungria, A. Martínez-Arias, M. Fernández-García, A. Iglesias-Juez, A. Guerrero-Ruiz, J. Calvino, J. C. Conesa and J. Soria, Chem. Mater. 15 (2003), 4309.

[25] D. I. Enache, D. W. Knight, G. J. Hutchings, Catal. Letters, 103 (2005), 43.

[26] X. Zheng,, X. Zhang, X. Wang, S. Wang, S. Wu, Appl. Catal. A: General 295 (2005), 142.

[27] S. M. Zhang, W. P. Huang, X. H. Qiu, B.Q. Li, X. C. Zheng, S. H. Wu, Catal. Letters, 80 (2002), 41.

[28] A. Martínez-Arias, M. Fernández-García, J. Soria, and J. C. Conesa, J. Catal., 182 (1999), 367.

[29] X.Q. Wang, J.A. Rodriguez, J.C. Hanson, D. Gamarra, A. Martínez-Arias and M. Fernández-García, J. Phys. Chem. B, 110 (2006), 428.

[30] F. Zhang, Q. Jin, S.-W. Chan, J. Appl. Phys. 95 (2004), 4319.

[31] PDF #34-0394, JCPDS Powder Diffraction File, Int. Center for Diffraction Data, Swarthmore, PA, 1993.

[32] L.-S. Kau, D. J. Solomon, J. E. Penner-Haln, K. O. Hodgson, E. I. Solomon, J. Am. Chem. Soc. 109 (1987), 6433.

[33] B.Skårman, D.Grandjean, R. E. Benfield, A. Hinz, A. Andersson, L. R. Wallenberg, J. Catal. 211(2002), 119, and references therein.

[34] X.D. Ma, T. Yokoyama, T, Hozumi, K. Hashimoto, S. Ohkoshi, Phys. Review B, 72 (2005), 094107.

[35] M. M. Günter, T. Ressler, R. E. Jentoft, and B. Bems, J. Catal., 203 (2001), 133.

[36] M. Fernández-García, Catal. Rev.-Sci. Eng. 44 (2002), 59.

[37] K. Otsuka, M. Hatano, A. Morikawa, J. Catal., 79 (1983), 493.

[38] F. Sadi, D. Duprez, F. Gérard, A. Miloudi, J. Catal. 213 (2003), 226.

[39] A. Trovarelli, Catal. Rev. Sci. Eng. 38 (1996), 439.

[40] H.C. Yao, Y.F. Yao, J. Catal., 86 (1984), 254.

[41] B. Engler, E. Koberstein, P. Schubert., Appl. Catal., 48 (1989), 71.

[42] J. A. Rodriguez, in: Dekker Encyclopedia of Nanoscience and Nanotechnology (Dekker, New York, 2004) pages 1297-1304.

[43] M. Haruta, Catal. Today, 36 (1997), 153.

[44] Q. Fu, H. Saltsburg, M. Flytzani-Stephanopoulos, Science, 301 (2003), 935.

[45] M. S. Chen, D. W. Goodman, Science, 306 (2004) , 252.

[46] C. T. Campbell, Science, 306 (2004) , 234.

[47] X.Q. Wang, J.A. Rodriguez, J.C. Hanson, M. Pérez, and J. Evans, J. Chem. Phys. 123 (2005), 221101.

[48] J. A. Rodriguez, M. Pérez, J. Evans, G. Liu, J. Hrbek, J. Chem. Phys. 122 (2005), 241101.

[49] Q. Fu, W. Deng, H. Saltsburg, M. Flytzani-Stephanopoulos, Appl. Catal. B: Environmental, 56 (2005) , 57.

[50] S. Carrettin, J. Guzman, A. Corma, Angew. Chem. Int. Ed., 44 (2005) , 2242.

[51] J. Guzman, and B. C. Gates, J. Am. Chem. Soc., 126 (2004) , 2672.

[52] M. Valden, X. Lai, D. W. Goodman, Science, 281 (1998) , 1647.

[53] D. W. Goodman, Catal. Lett. 99 (2005) , 1.

[54] J. A. Rodriguez, G. Liu, T. Jirsak, J. Hrbek, Z. Chang, J. Dvorak, A. Maiti, J. Am. Chem. Soc. 124 (2002) , 5242.

[55] A. Vijay, G. Mills, H. Metiu, J. Chem. Phys. 118 (2003) , 6536.

[56] H. Häkkinen, S. Abbet, A. Sanchez, U. Heiz, U. Landman, Angew. Chem. Int. Ed. 42 (2003), 1297.

[57] I. N. Remediakis, N. Lopez, J. K. Nørskov, Angew. Chem. Int. Ed., 44 (2005) , 1824.

[58] a) X.Q. Wang, J. C. Hanson, G. Liu, J. A. Rodriguez, A. Iglesias-Juez, M. Fernández-García, J. Chem. Phys. 121 (2004) , 5434. b) X.Q. Wang, J. C. Hanson, A. I. Frenkel, J. –Y. Kim, J. A. Rodriguez, J. Phys. Chem. B, 108 (2004) , 13667. c) X.Q. Wang, J. C. Hanson, G. Liu, J. A. Rodriguez, C. Belver, M. Fernández-García, J. Chem. Phys. 122 (2005), 154711.

[59] P. Norby, J. C. Hanson, Catal. Today, 39 (1998) , 301.

[60] P. J. Chupas, M. F. Ciraolo, J. C. Hanson, C. P. Grey, J. Am. Chem. Soc., 123 (2001), 1694.

[61] a) V. Schwartz, D. R. Mullins, W. Yan, B. Chen, S, Dai , S. H. Overbury, J. Phys. Chem. B, 108 (2004) , 15782. b) G. Jacobs, S. Ricote, P.M. Patterson, U.M. Graham, A. Dozier, S. Khalid, E. Rhodus and B.H. Davis, Appl. Catal. A: General, 292 (2005), 229.

[62] J. A. Rodriguez, X.Q. Wang, G. Liu, J. C. Hanson, J. Hrbek, C. H. F. Peden, A. Iglesias-Juez, M. Fernández-García, J. Molecular Catal. A: Chemical, 228 (2005) , 11.

[63] C.T. Campbell and K.A. Daube, J. Catal. 104 (1987) , 109.

[64] J.A. Rodriguez, T. Jirsak, A. Freitag, J.C. Hanson, J.Z. Larese, S. Chaturvedi, Catal. Lett. 62 (1999) , 113.

[65] R. M. Ferriz, R. J. Gorte, J. M. Vohs, Catal. Lett. 82 (2002), 123.

[66] a) G. Liu, J.A. Rodriguez, J. Hrbek, J. Dvorak, and C.H.F. Peden, J. Phys. Chem. B, 105 (2001), 7762. b) J.Z. Shyu, W.H. Weber and H.S. Gandhi, J. Phys. Chem. 92 (1988), 4964.

[67] J. Nakamura, J.M. Campbell and C.T. Campbell, J. Chem. Soc. Faraday 86 (1990), 2725.

[68] S. Oyama, T. Ito, J.A. Rodriguez, J. Nakamura, to be published.

[69] G. Jacobs, E. Chenu, P.M. Patterson, L. Williams, D. Sparks, G. Thomas and B.H. Davis, Applied Catal. A: General, 258 (2004), 203.

[70] L. Mendelovici and M. Steinberg, J. Catal. 96 (1985), 285.

[71] T. Bunluesin, R.J. Gorte, and G.W. Graham, Appl. Catal. B: Environ. 15 (1998), 107.

[72] S. Hilaire, X. Wang, T. Luo, R.J. Gorte and J. Wagner, Appl. Catal. A: Gen. 215 (2001), 271.

[73] E. Chenu, G. Jacobs, A.C. Crawford, R.A. Keogh, P.M. Patterson, D.E. Sparks, and B.H. Davis, Appl. Catal. B: Environ. 59 (2005), 45.

[74] S. Ricote, G. Jacobs, M. Milling, Y. Ji, P.M. Patterson, and B. Davis, Appl. Catal. A: General, 303 (2006), 35.

[75] A. Basinska, L. Kepinski and F. Domka, Appl. Catal. A: General, 183 (1999), 143.

[76] A.F. Ghenciu, Current Opinion in Solid State and Materials Science, 6 (2002), 389.

[77] M.A. Peña, J.P. Gómez, and J.L.G. Fierro, Appl. Catal. A: General, 144 (1996), 7.

[78] J.R. Rostrup-Nielsen, Catal. Today, 18 (1993), 305.

[79] R. Craciun, W. Daniel, and H. Knozinger, Appl. Catal. A: General, 230 (2002), 153.

[80] S.S. Bharadwaj and L.D. Schmidt, Fuel Process Technol. 42 (1995), 109.

[81] A.T. Ashcroft, A.K. Cheetham, M.L.H. Green and C.P. Grey, Nature, 344 (1990), 319.

[82] P. Pantu, K. Kim, G.R. Gavalas, Appl. Catal. A: General, 193 (2000), 203.

[83] W.S. Dong, K.W. Jun, H.S. Ro, Z.W. Liu, and S.E. Park, Catal. Lett. 78 (2002), 13.

[84] V.A. Sadykov and T.G. Kuznetsova, React. Kin. Catal. Lett. 76 (2002), 83.

[85] S. Bedrane, C. Descorme, and D. Duprez, Catal. Today, 75 (2002), 401.

[86] S. Velu, K. Suzuki, M.P. Kapoor, F. Ohashi and T. Osaki, Appl. Catal. A: General, 213 (2001), 47.

[87] I.P. Breen and J.R.H. Roos, Catal. Today, 51 (1999), 521.

[88] M. Marczewski and R. Peplonski, React. Kinec. Catal. Lett. 22 (1983), 241.

[89] J.P. Kreese, A. Antok, and R.T. Smith, private communication.

[90] A. Fujishima and K. Honda, Nature, 238 (1972), 37.

[91] M. Grätzel, Nature, 414 (2001), 338.

[92] H. Arakawa and K. Sayama, Catalysis Surveys from Japan, 4 (2000), 75.

[93] J.M. Bolts and M.S. Wrighton, J. Phys. Chem., 80 (1976), 2641.

[94] K. Domen, A. Kudo, and H. Onishi, J. Catal., 102 (1986), 92.

[95] R. Asahi, T. Morikawa, T. Ohwaki, K. Aoki, and Y. Taga, Science, 293 (2001), 269.

[96] X. Chen and C. Burda, J. Phys. Chem. B, 108 (2004), 15446.

[97] R. Nakamura, T. Tanaka and Y. Nakato, J. Phys. Chem. B, 108 (2004), 10617.

[98] C. Di Valentin, G. Pacchioni and A. Selloni, Phys. Rev. B, 70 (2004), 085116.

[99] J.Y. Lee, J. Park, and J.-H. Cho, Appl. Phys. Lett. 87 (2005), 011904.

[100] M. Batzill, E. Morales and U. Diebold, Phys. Rev. Lett. 96 (2006), 026103.

[101] X. Li and I. Sabir, International J. Hydrogen Energy. 30 (2005), 359.

[102] V. Metha and J.S. Cooper, J. Power Sources, 114 (2003), 32.

[103] B. Smitha, S. Sridhar, and A.A. Khan, J. Membrane Sciences, 259 (2005), 10.

[104] S. Fukui, T. Naito, and Q. Li, private communication.

[105] J. Schoonman, Solid State Ionics, 135 (2000), 5.

[106] R. Farrauto, S. Hwang, L. Shore, W. Ruettinger, L. Lampert, T. Giroux. Y. Liu, O. Ilinich, Annual Review of Materials Research, 33 (2003), 1.

[107] L.J.M.J. Blomen, M.N. Mugerwa, Fuel Cell Systems, Plenum Press, 1993.

[108] P.N. Ross, N.M. Markovic, T.J. Schmidt, V. Stammenkovic, New Electrocatalysts for Fuel Cells, Transportation Fuel Cell Power System, 2000 Annual Progress Report, 200, 115.

[109] S. Litster, G. McLean, J. Power Sources, 130 (2004), 61.

[110] S.C. Singhal and K. Kendall, High Temperature Solid Oxide Fuel Cells: Fundamentals, Design and Applications (Oxford, UK, Elsevier Ltd, 2003).

[111] S.C. Singhal, Solid State Ionics, 135 (2000), 305.

[112] S.P.S. Badwal, Solid State Ionics, 143 (2001), 39.

[113] T. Fukui, S. Ohara, M. Naito and K. Nogi, J. of Nanoparticle Research, 3 (2001), 171.

[114] S.P. Jiang and S.H. Chan, Journal of Materials Science, 39 (2004), 4405.

[115] A) F. Besenbacher, I. Chorkendorff, B. S. Clausen, B. Hammer, A. M. Molenbroek, J. K. Norskov, and I. Stensgaard, Science, 279 (1998), 1913. b) J. R. Rostrup-Nielsen, Catalyst deactivation, in: C.H. Bartholomew, J. B. Butt (Eds.), Studies in Surface Science and Catalysis, vol. 68, Elsevier, Amsterdam, 1991. c) H. S. Bengaard, J. K. Norskov, J. Sehested, B. S. Clausen, L. P. Nielsen, A. M. Molenbroek, and J. R. Rostrup-Nielsen, J Catal. 209 (2002), 365.

[116] Y. H. Hu and E. Ruckenstein, Catal. Reviews, 44(3) (2002), 423.

[117] D. L. Trimm, Catal. Today, 49(1999**)**, 3.

[118] T. Takeguchi, R. Kikuchi, T. Yano, K. Eguchi, and K. Murata, Catal. Today, 84 (2003), 217.

[119] T. Takeguchi, T. Yano, Y. Kani, R. Kikuchi, and K. Eguchi, in "SOFC-VIII", edited by S.C. Singhal and M. Dokiya (Electrochem. Soc., Pennington, NJ, 2003) Vol. 2003-07, p.704.

[120] K. Eguchi, T. Setoguchi, K. Okamoto and H. Arai, in Proc. of the International Fuell Cell Conf. (Makihari, Japan, 1992) p. 373.

[121] S. Park and J. Kim, to be published.

[122] S.D. Park, J.M. Vohs, and R.J. Gorte, Nature, 404 (2000), 265.

[123] H. Kim, C. Lu, W.L. Worrell, J.M. Vohs and R.J. Gorte, J. Electrochem. Soc. 149 (2002), A247.

[124] R.J. Gorte, H. Kim and J.H. Vohs, J. Power Sources, 106 (2002), 10.

Figure Captions:

Figure 1: H_2 production pathways

Figure 2: Different types of fuel cells (from Ref. 11a)

Figure 3. a) Time-resolved X-ray diffraction patterns for a $Ce_{0.95}Cu_{0.05}O_2$ catalyst during the water gas shift reaction at different temperatures (λ = 0.922 Å). b) The relative concentration of H_2 produced as a function of time at different temperatures during the water gas shift reaction as shown in part a.

Figure 4. Cu K-edge XANES (part a) and EXAFS spectra (part b) collected over $Ce_{0.95}Cu_{0.05}O_2$ catalyst cooled down to room temperature after the water gas shift reaction at different temperatures.

Figure 5. a) Cu K-edge XANES spectra collected over a $Ce_{0.8}Cu_{0.2}O_2$ catalyst cooled down to room temperature after the water gas shift reaction at the indicated temperatures. b) Ce L_3-edge XANES spectra collected over $Ce_{0.8}Cu_{0.2}O_2$ during the water gas shift reaction at different temperatures.

Figure 6. a) Ceria lattice parameters during gas-switch experiments over a $Ce_{0.8}Cu_{0.2}O_2$ catalyst at 400^{o}C. b) Ceria lattice parameters of $Ce_{0.8}Cu_{0.2}O_2$ in the gas-switch experiments as a function of temperature.

Figure 7. XRD patterns for ceria impregnated with copper oxides (top two traces, 3% and 5% Cu in weight) and $Ce_{1-x}Cu_xO_2$ samples (bottom three traces). (λ = 0.922 Å) [13]

Figure 8. Cu K-edge XANES spectra collected over 5%CuOx/CeO_2 catalyst cooled down to room temperature after the water gas shift reaction at the indicated temperatures.

Figure 9. Ceria lattice parameters in gas-switch experiments over a 5%CuOx/CeO_2 sample at 400^{o}C.

Figure 10. Top panel: Relative amounts of H_2 and CO_2 formed during the WGS reaction on a 2.4wt%Au-Ce(10at%Gd)O_x catalyst. A mixture of 5%CO and 3%H_2O in He (total flow ~ 10 ml/min) was passed over the catalyst at 300, 400 or 500 ^oC. Bottom panel: X-ray diffraction patterns collected *in situ* during the WGS on the 2.4wt%Au-Ce(10at%Gd)O_x catalyst. For comparison, we are also including the XRD pattern for a fresh catalyst with 5wt%Au, dashed trace.

Figure 11. Au L_3-edge XANES spectra collected *in situ* during the WGS reaction over a 2.4wt%Au-CeO_2 catalyst. The sample was exposed to a mixture of 5%CO and 3%H_2O in He (total flow ~ 10 ml/min) at the indicated temperatures. For comparison, we also include the spectra for a fresh 0.5wt%Au-CeO_2 catalyst, dashed trace, and a gold foil.

Figure 12. Au 4f core-level photoemission spectra collected before and after exposing a AuO_x/CeO_2 interface (θ_{Au} ~ 0.15 monolayer) to a mixture of 5 Torr of CO and 10 Torr of H_2O at 300 ^oC for 5 min.

Figure 13. Top panel: Amounts of H_2 and CO_2 produced during the WGS reaction on reduced Au/CeO_2(111) and AuO_x/CeO_2 (θ_{Au} ~ 0.15 monolayer) catalysts. The catalysts were pre-conditioned as described in the text. Then, they were exposed to a mixture of 20 Torr of CO and 10 Torr of H_2O at 350 ^oC for 5 min in a batch reactor. The amounts of H_2 and CO_2 produced during this time period are plotted in the graph. Bottom panel: Amounts of H_2 and CO_2 produced during the WGS reaction on reduced Au/CeO_2(111) catalysts with different Au coverages. After pre-conditioning (see text), each surface was exposed to a mixture of 20 Torr of CO and 10 Torr of H_2O at 350 ^oC for min.

Figure 14. Ceria lattice parameters determined from TR-XRD patterns for a 2.4wt%Au-Ce(10at%Gd)O_x catalyst under different gases at 500 ^oC: pure He, 5% CO in He, 5% CO and 3% H_2O in He, again 5% CO in He, and finally 5% O_2 in He.

Figure 15. CO conversions for the WGS reaction at 400^oC over CuO, 5%CuOx/CeO_2, $Ce_{0.8}Cu_{0.2}O_2$, $Ce_{0.95}Cu_{0.05}O_2$ and 2.4wt%AuOx/CeO_2 catalysts with the same operating conditions (Space velocity ~ $1.5x10^5$/h, ~5mg of catalyst).

Figure 16. PEMFC schematic diagram. (from Ref. 109)

Figure 17. Tubular configuration of SOFC.

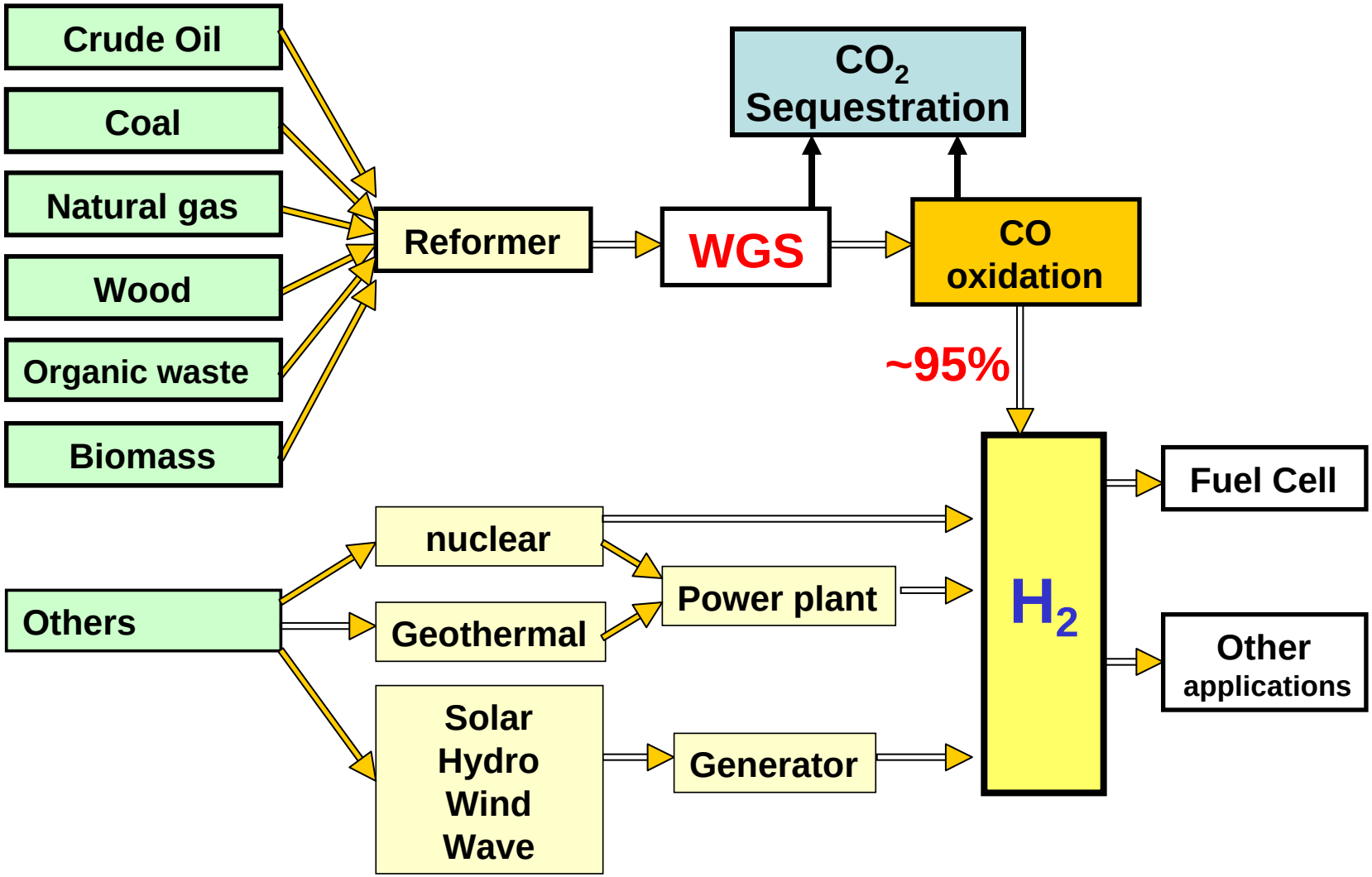
Crude Oil
Coal
Natural gas
Wood
Organic waste
Biomass
Reformer
WGS
CO_2 Sequestration
CO oxidation
~95%
H_2
Fuel Cell
Other applications
nuclear
Power plant
Geothermal
Others
Solar
Hydro
Wind
Wave
Generator

Fig.1

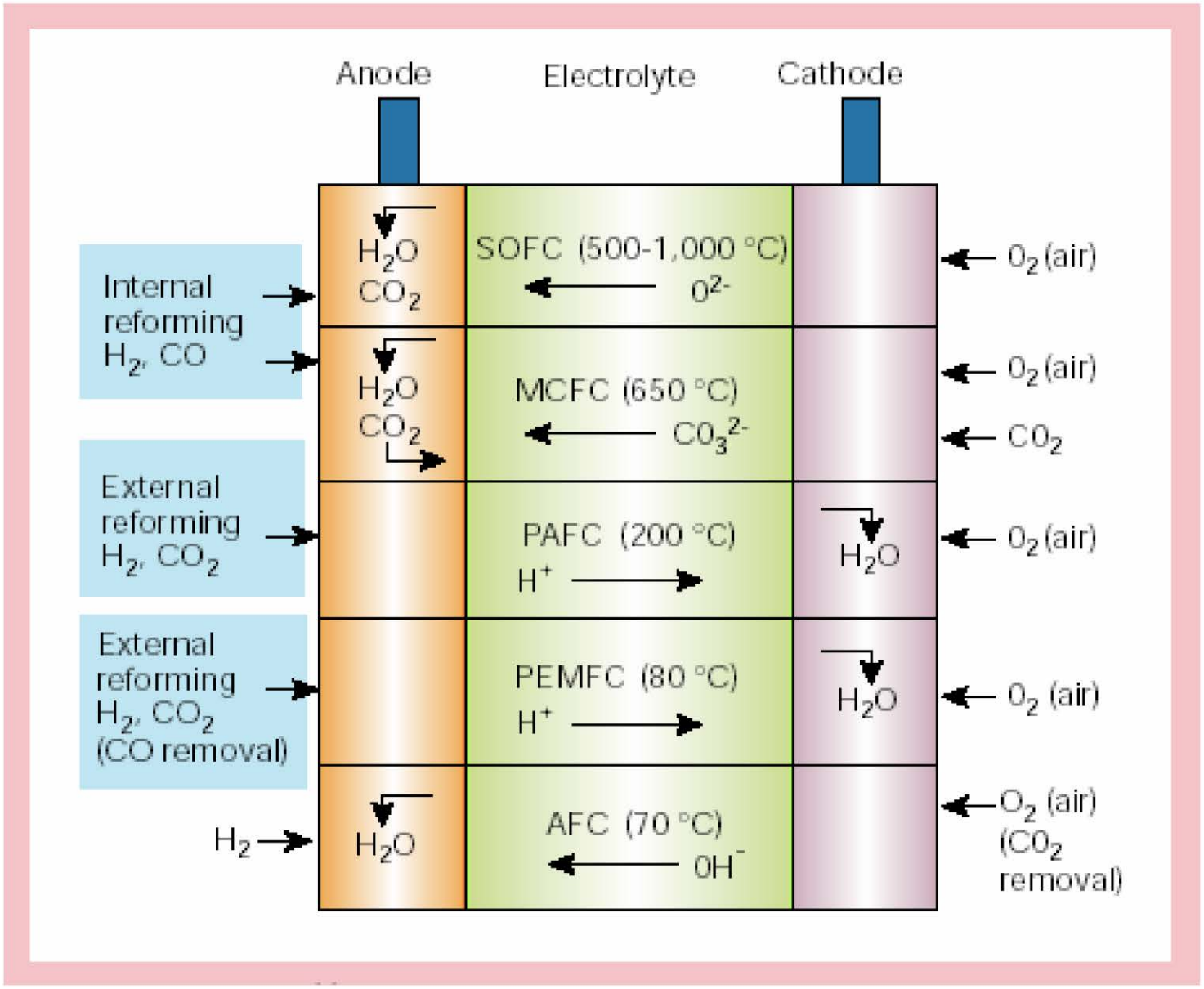
Anode
Electrolyte
Cathode
Internal reforming H_2, CO
External reforming H_2, CO_2
External reforming H_2, CO_2 (CO removal)
H_2
H_2O
CO_2
SOFC (500-1,000 °C)
O^{2-}
MCFC (650 °C)
CO_3^{2-}
PAFC (200 °C)
H^+
PEMFC (80 °C)
H^+
AFC (70 °C)
OH^-
O_2 (air)
CO_2
O_2 (CO_2 removal)

Fig.2

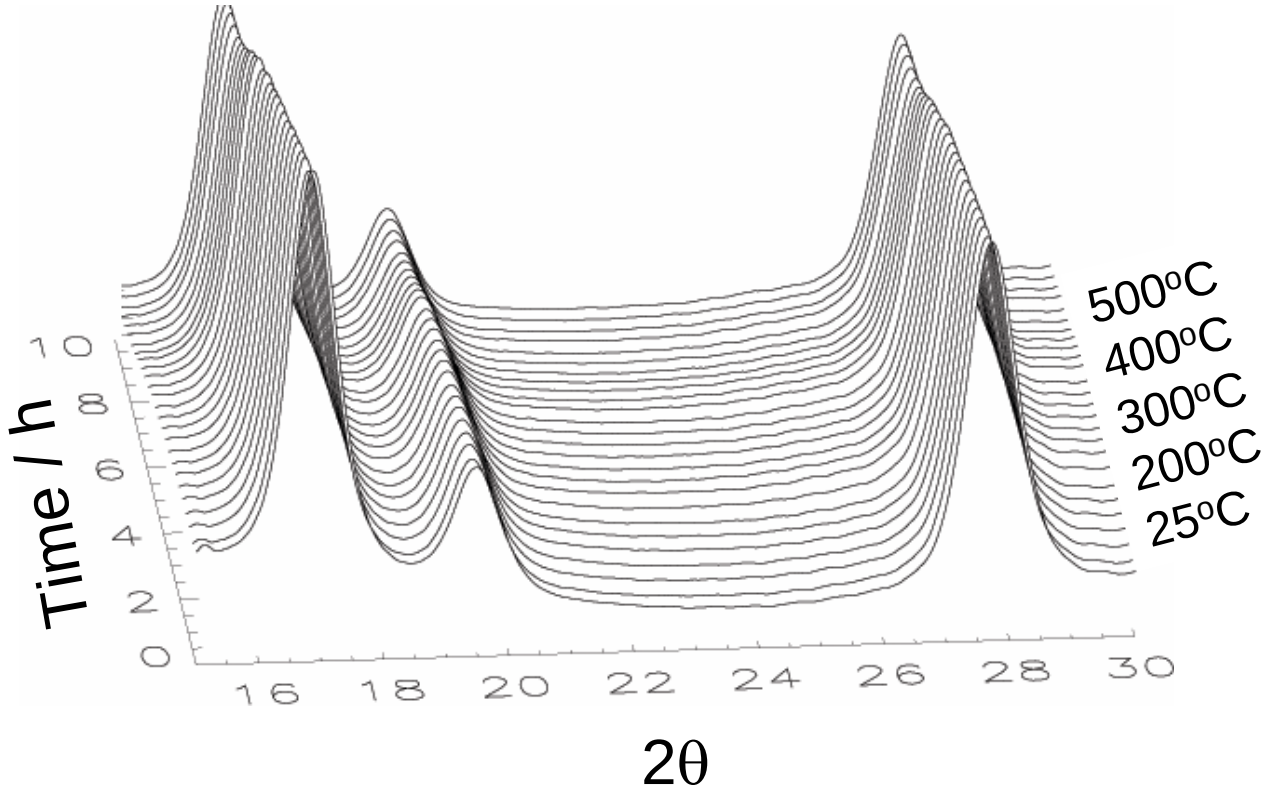
Time / h
0
2
4
6
8
10
16
18
20
22
24
26
28
30
2θ
500°C
400°C
300°C
200°C
25°C

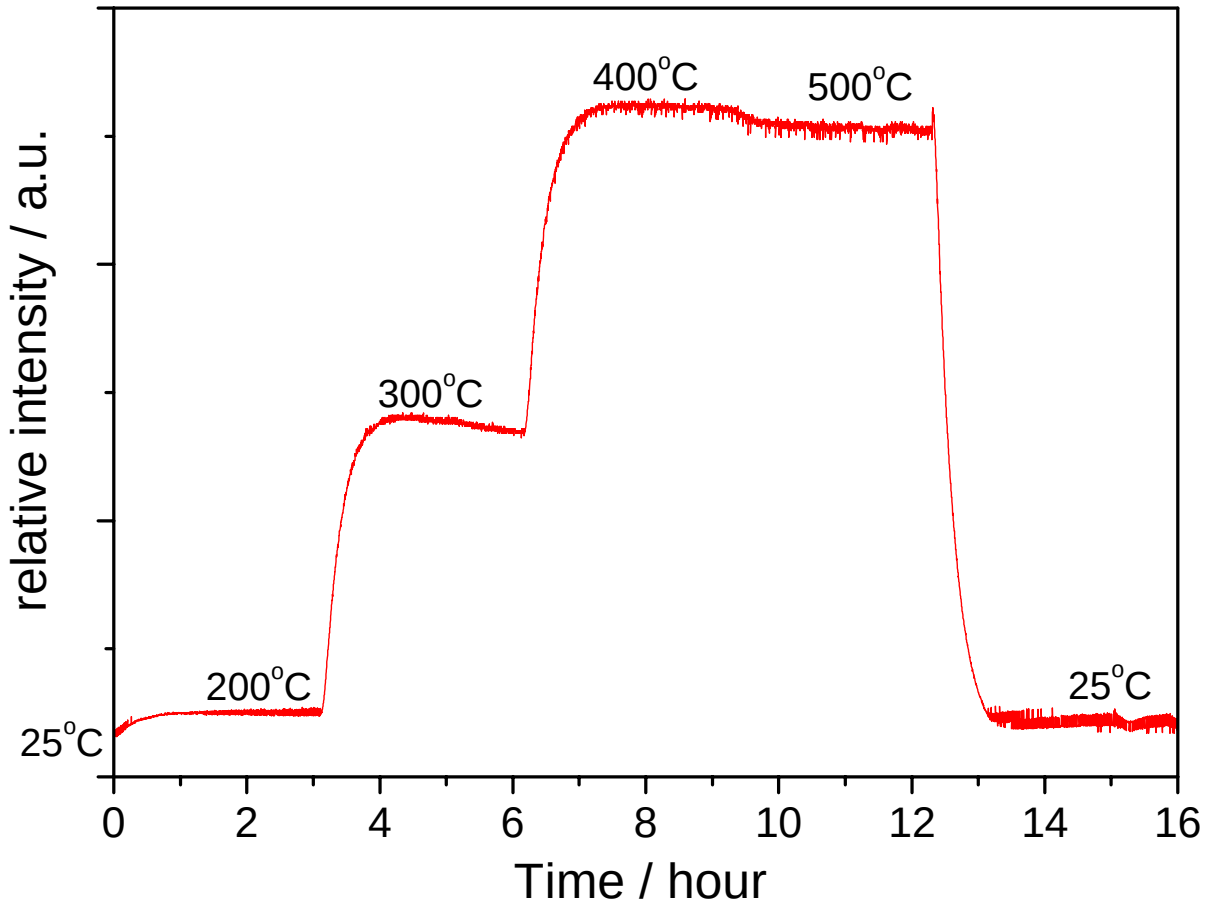
relative intensity / a.u.
25°C
200°C
300°C
400°C
500°C
25°C
0
2
4
6
8
10
12
14
16
Time / hour

Fig. 3

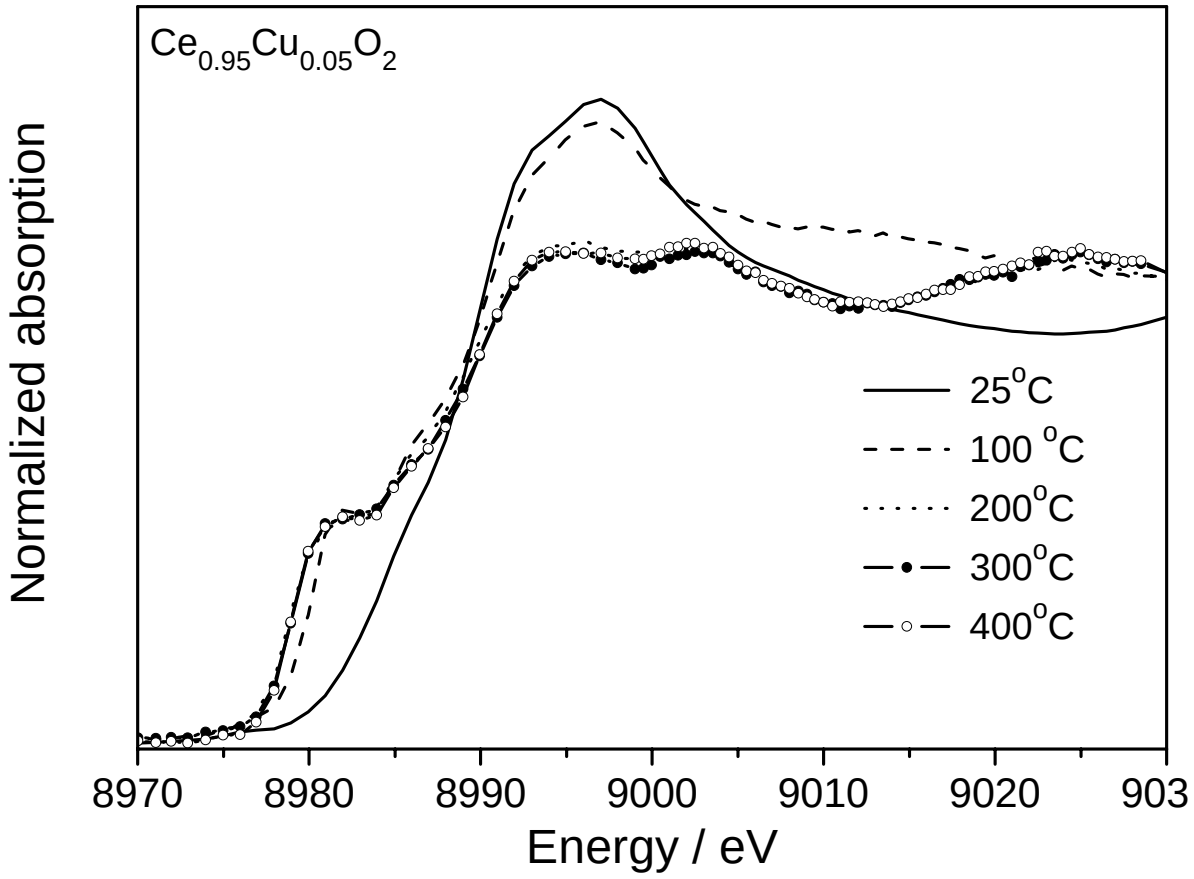
Ce0.95Cu0.05O2
Normalized absorption
25°C
100 °C
200°C
300°C
400°C
8970
8980
8990
9000
9010
9020
903
Energy / eV

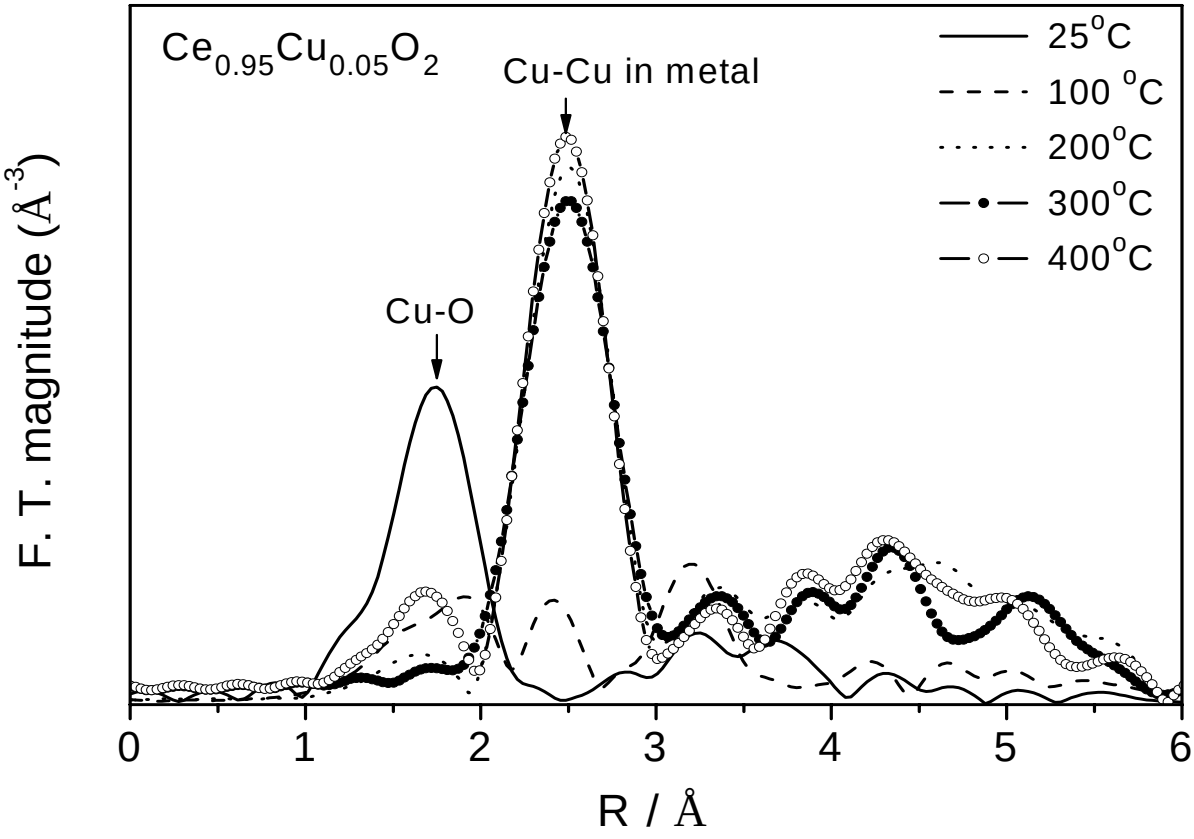
Ce0.95Cu0.05O2
Cu-Cu in metal
Cu-O
F. T. magnitude (Å-3)
25°C
100 °C
200°C
300°C
400°C
0
1
2
3
4
5
6
R / Å

Fig. 4

a)

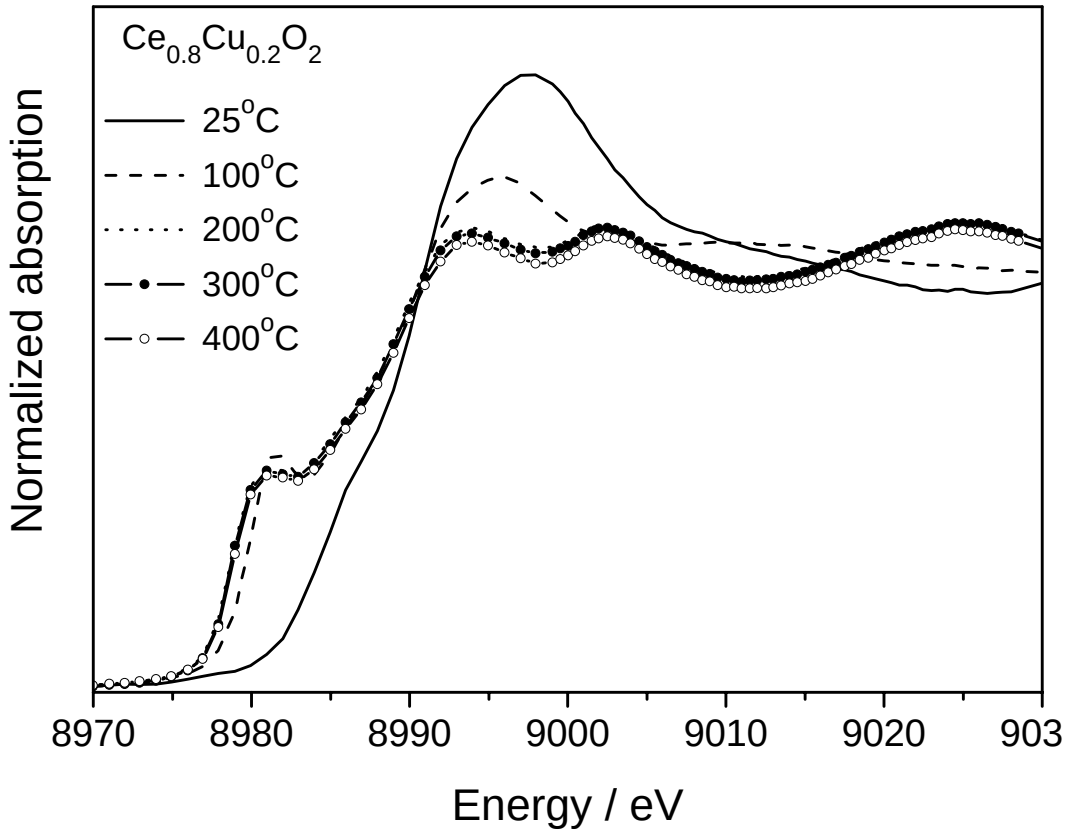
Ce0.8Cu0.2O2
25oC
100oC
200oC
300oC
400oC
Normalized absorption
8970
8980
8990
9000
9010
9020
903
Energy / eV

b)

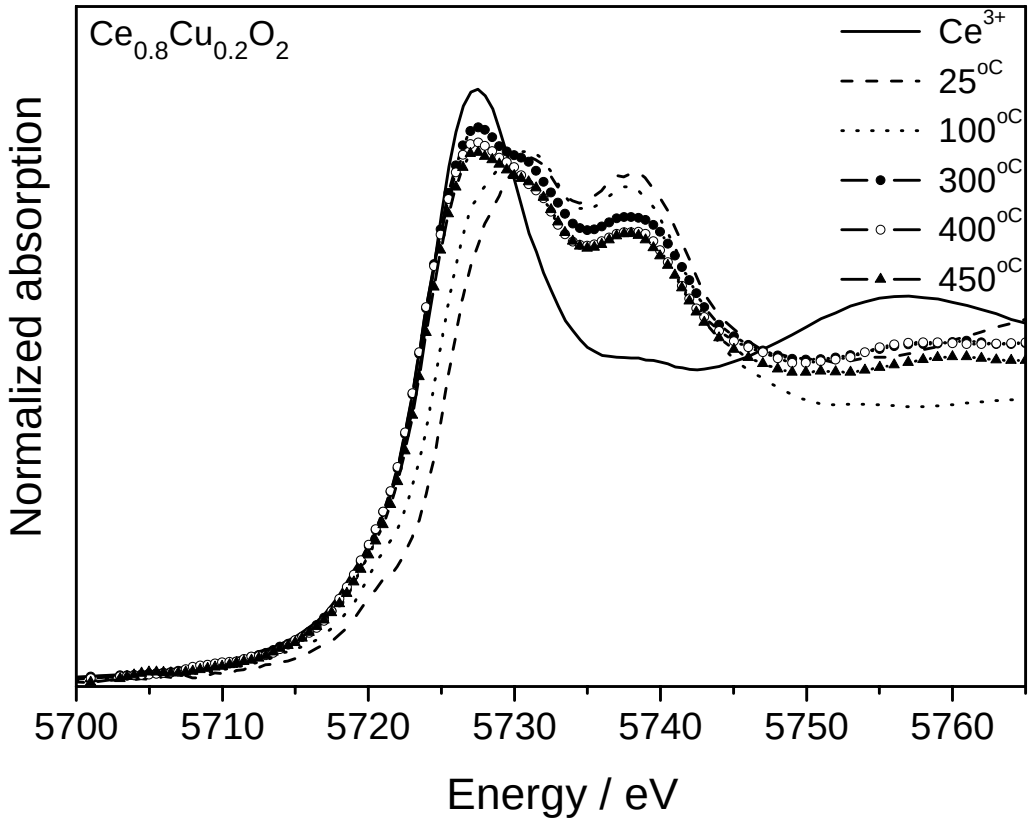
Ce0.8Cu0.2O2
Ce3+
25oC
100oC
300oC
400oC
450oC
Normalized absorption
5700
5710
5720
5730
5740
5750
5760
Energy / eV

Fig.5

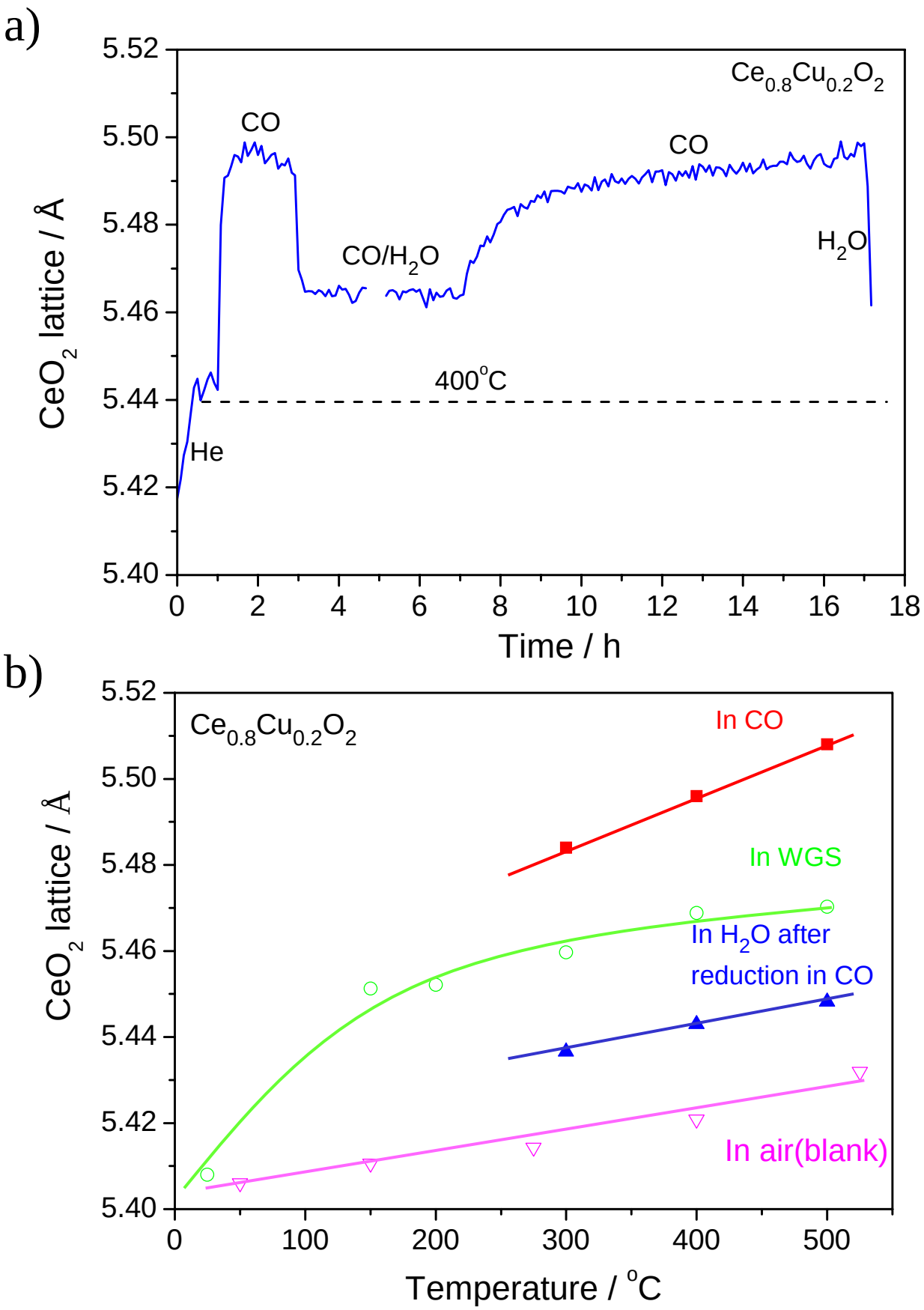
a)
$Ce_{0.8}Cu_{0.2}O_2$
CO
CO
CO/H_2O
H_2O
400°C
He
CeO_2 lattice / Å
Time / h
b)
$Ce_{0.8}Cu_{0.2}O_2$
In CO
In WGS
In H_2O after reduction in CO
In air(blank)
CeO_2 lattice / Å
Temperature / °C

Fig.6

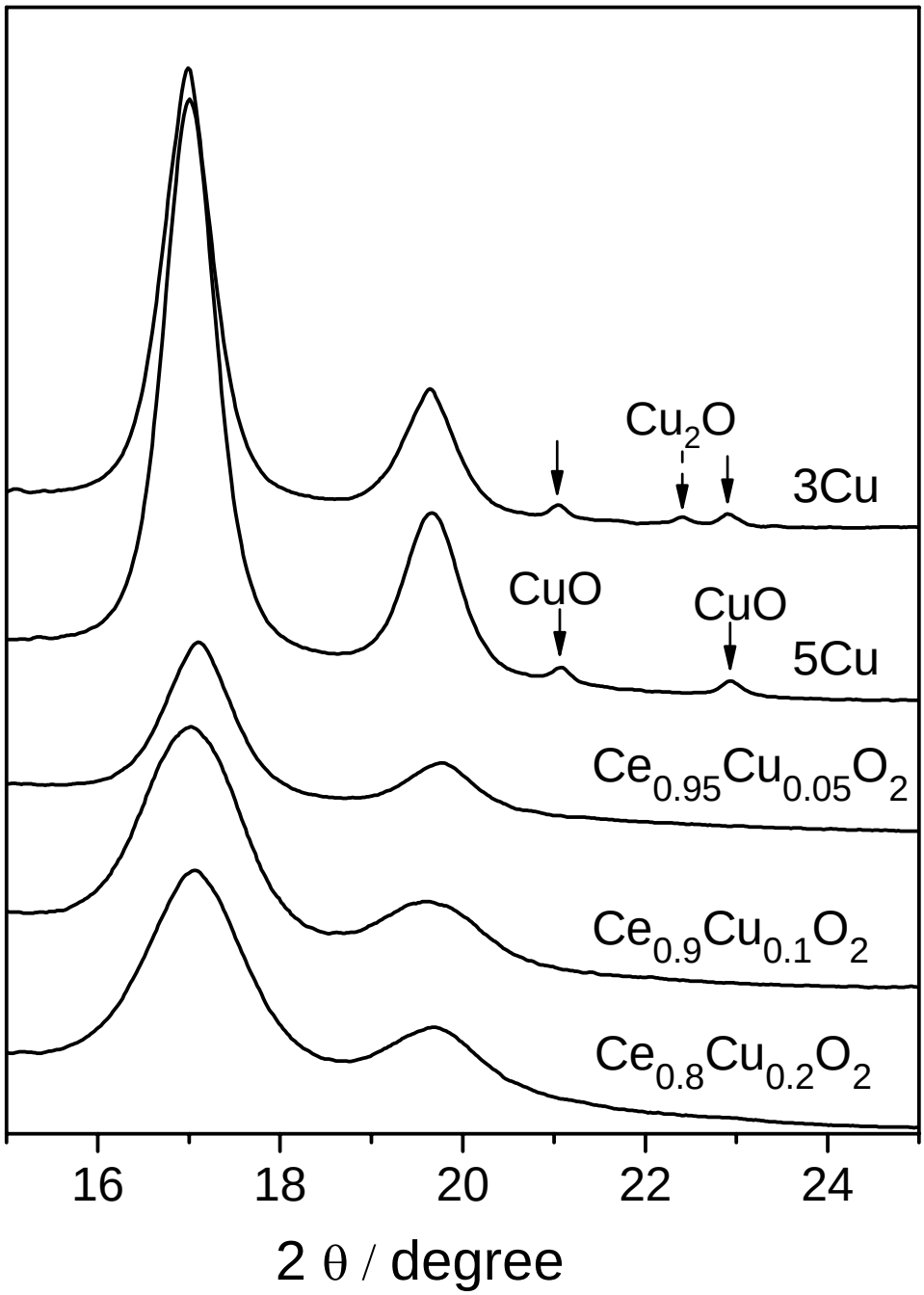
Cu2O
3Cu
CuO
CuO
5Cu
Ce0.95Cu0.05O2
Ce0.9Cu0.1O2
Ce0.8Cu0.2O2
16
18
20
22
24
2 θ / degree

Fig.7

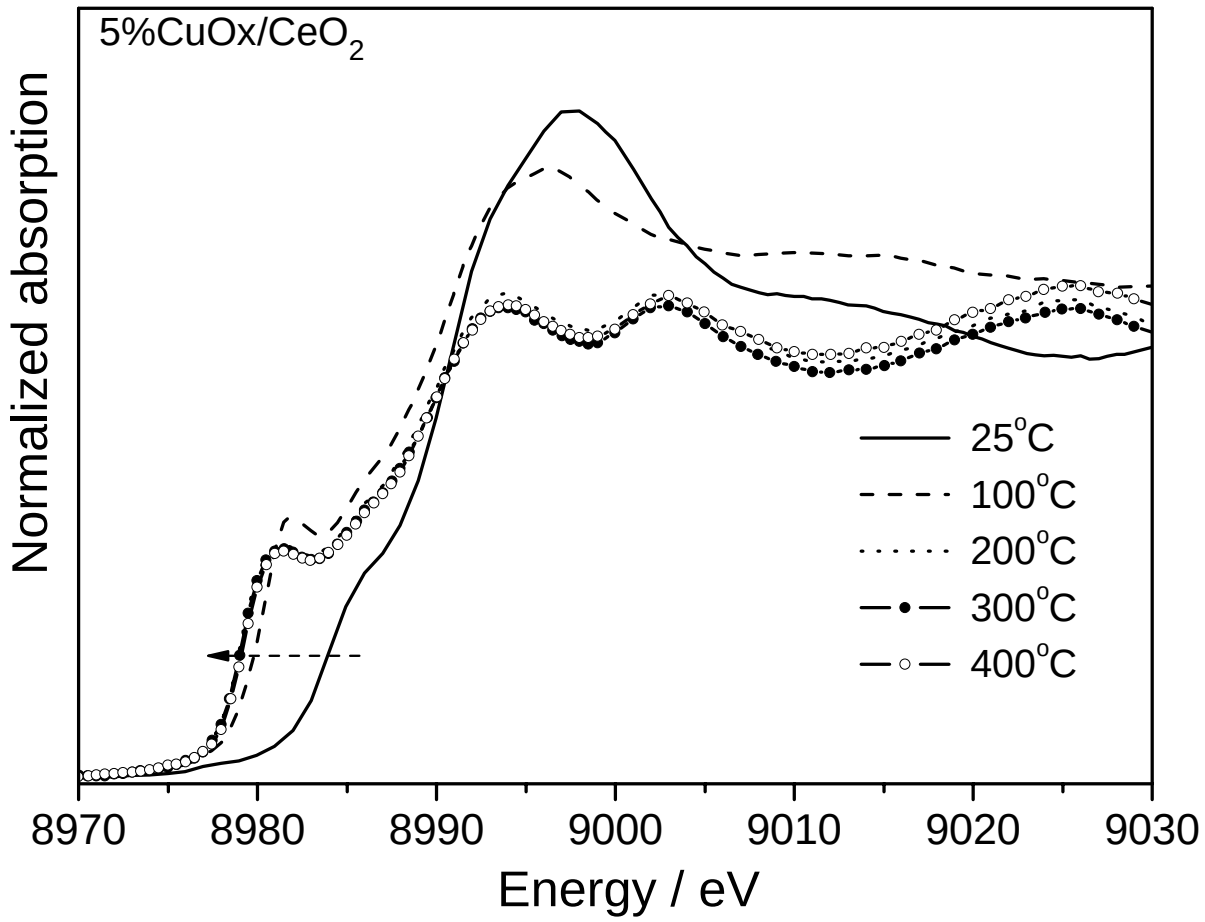
5%CuOx/CeO2
Normalized absorption
Energy / eV
8970
8980
8990
9000
9010
9020
9030
25°C
100°C
200°C
300°C
400°C

Fig.8

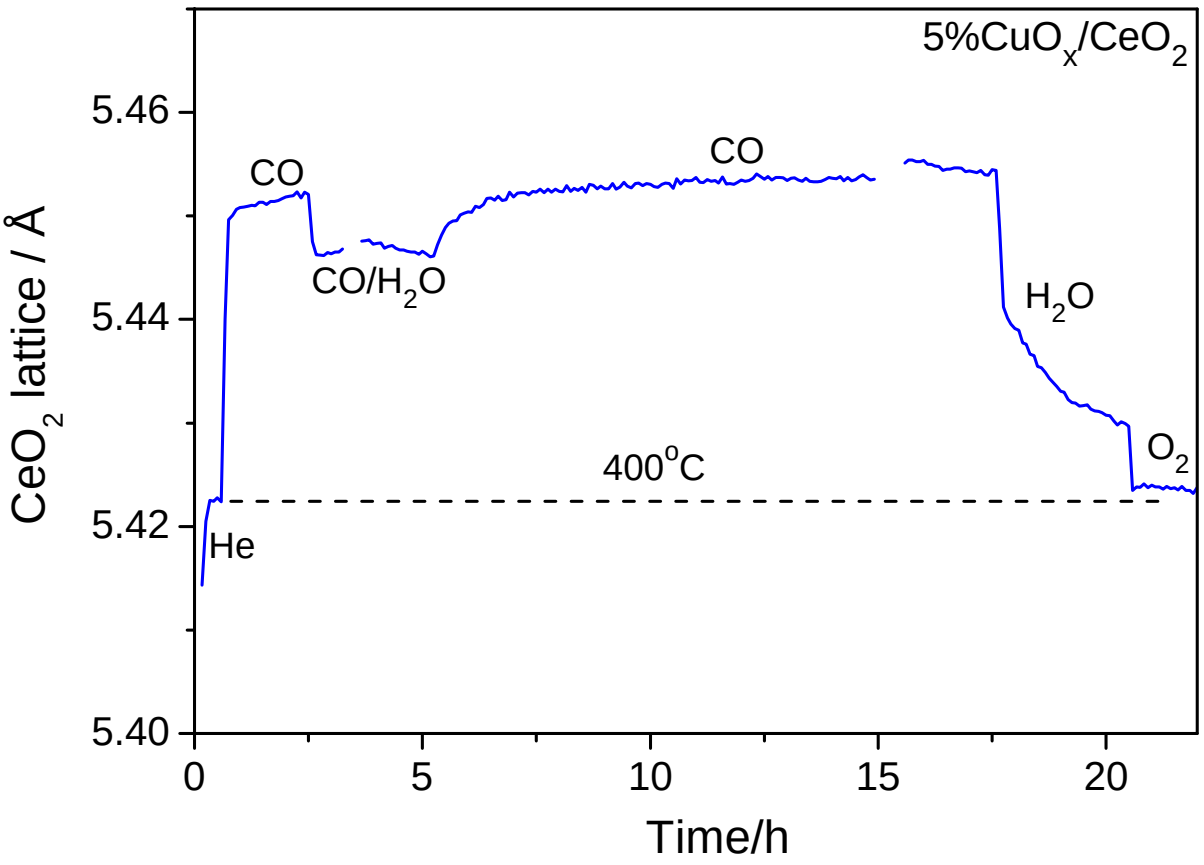
5%CuO$_x$/CeO$_2$
CeO$_2$ lattice / Å
5.46
5.44
5.42
5.40
0
5
10
15
20
Time/h
CO
CO/H$_2$O
CO
H$_2$O
O$_2$
400°C
He

Fig.9

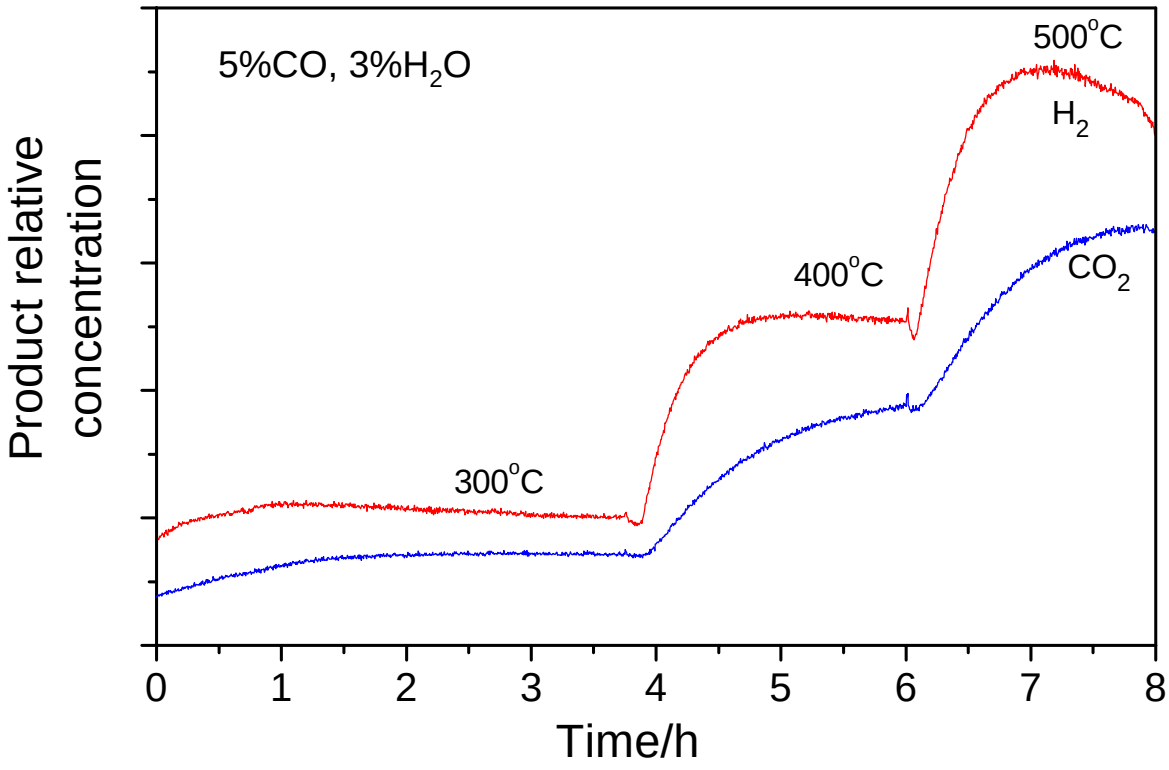
5%CO, 3%H2O
500°C
H2
400°C
CO2
300°C
Product relative concentration
0
1
2
3
4
5
6
7
8
Time/h

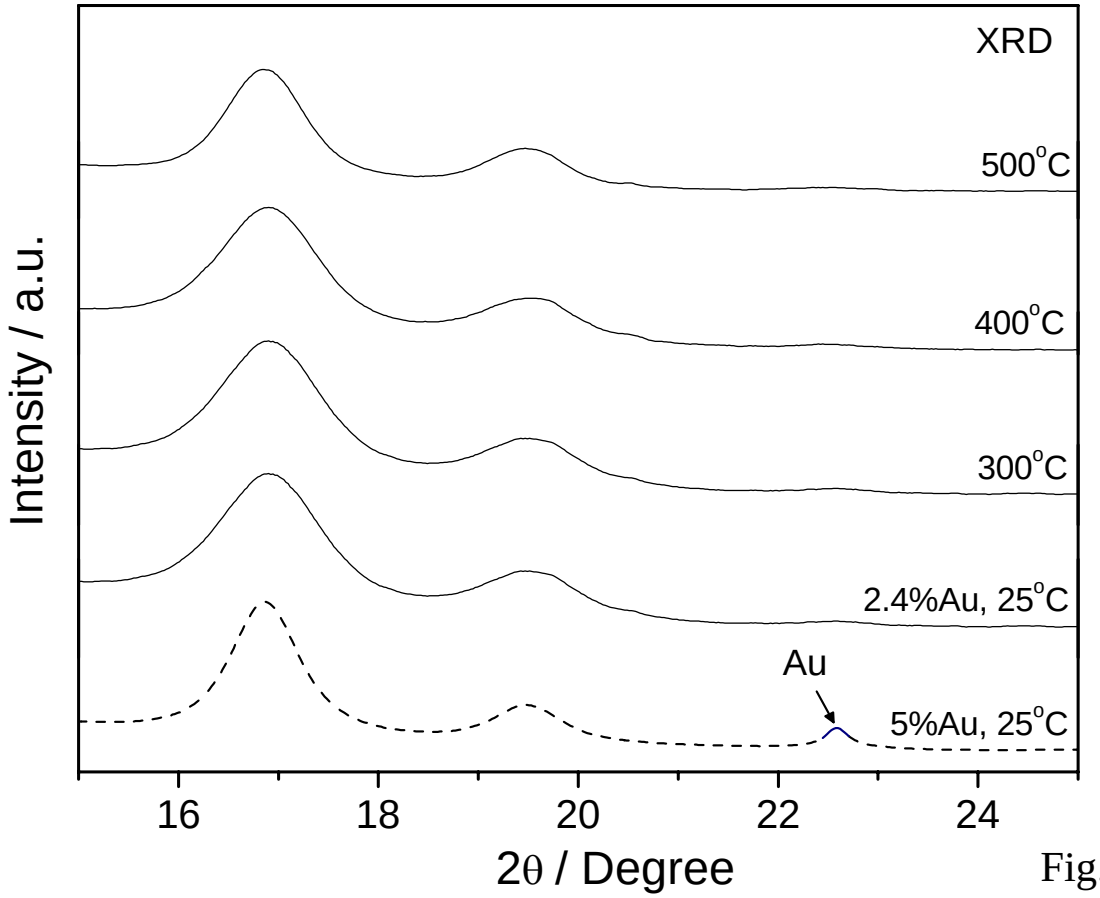
XRD
500°C
400°C
300°C
2.4%Au, 25°C
Au
5%Au, 25°C
Intensity / a.u.
16
18
20
22
24
2θ / Degree

Fig. 10

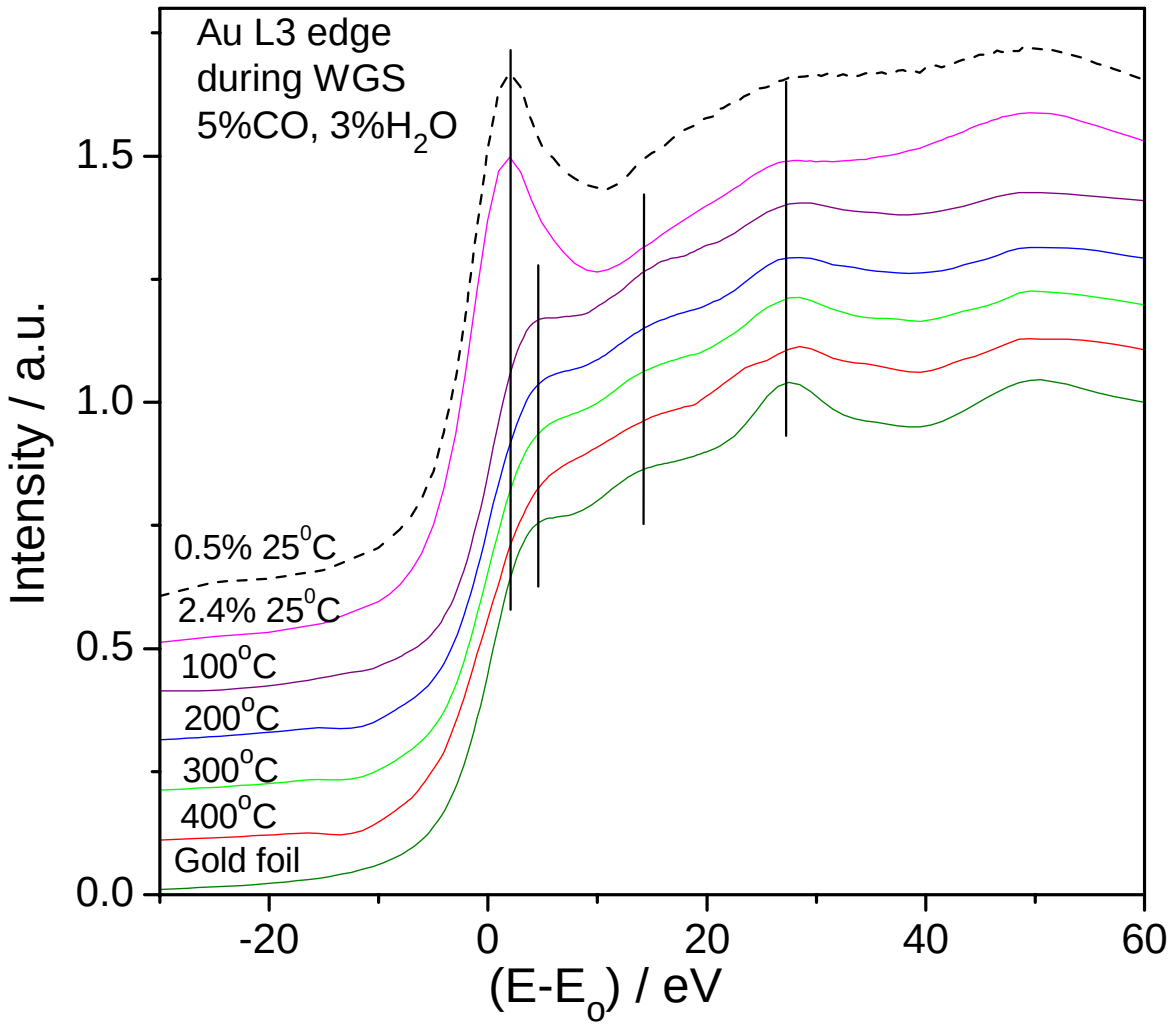
Au L3 edge
during WGS
5%CO, 3%H2O
0.5% 25°C
2.4% 25°C
100°C
200°C
300°C
400°C
Gold foil
Intensity / a.u.
(E-E0) / eV
0.0
0.5
1.0
1.5
-20
0
20
40
60

Fig.11

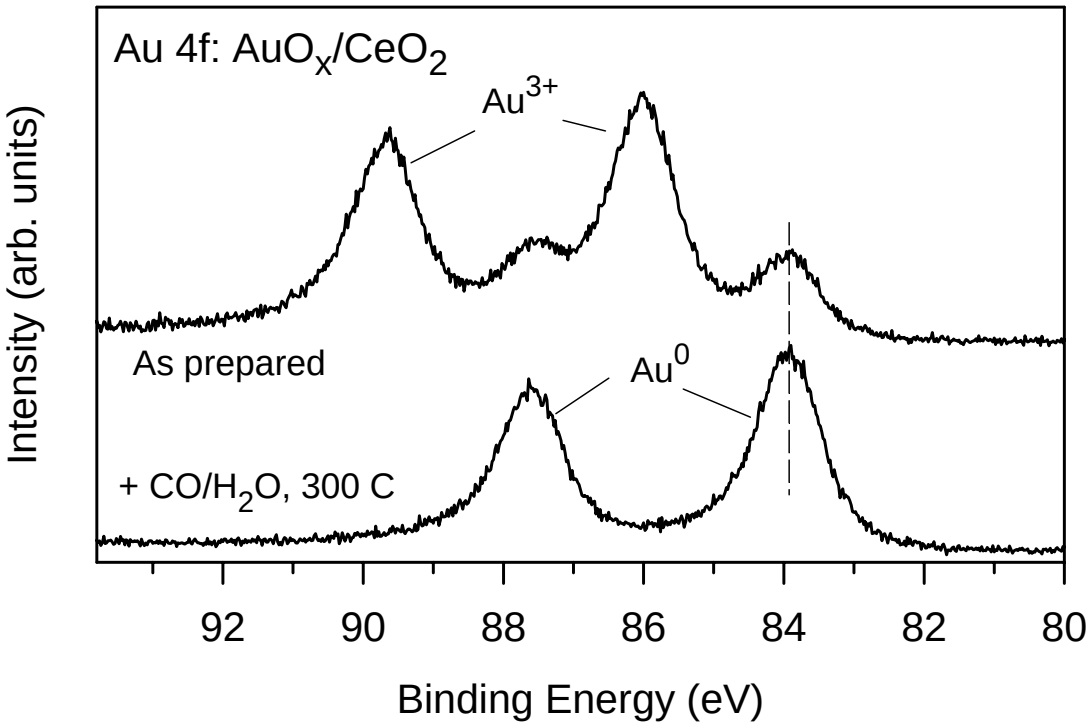
Au 4f: AuO$_x$/CeO$_2$
Au^{3+}
As prepared
Au^0
+ CO/H$_2$O, 300 C
Intensity (arb. units)
92
90
88
86
84
82
80
Binding Energy (eV)

Fig. 12

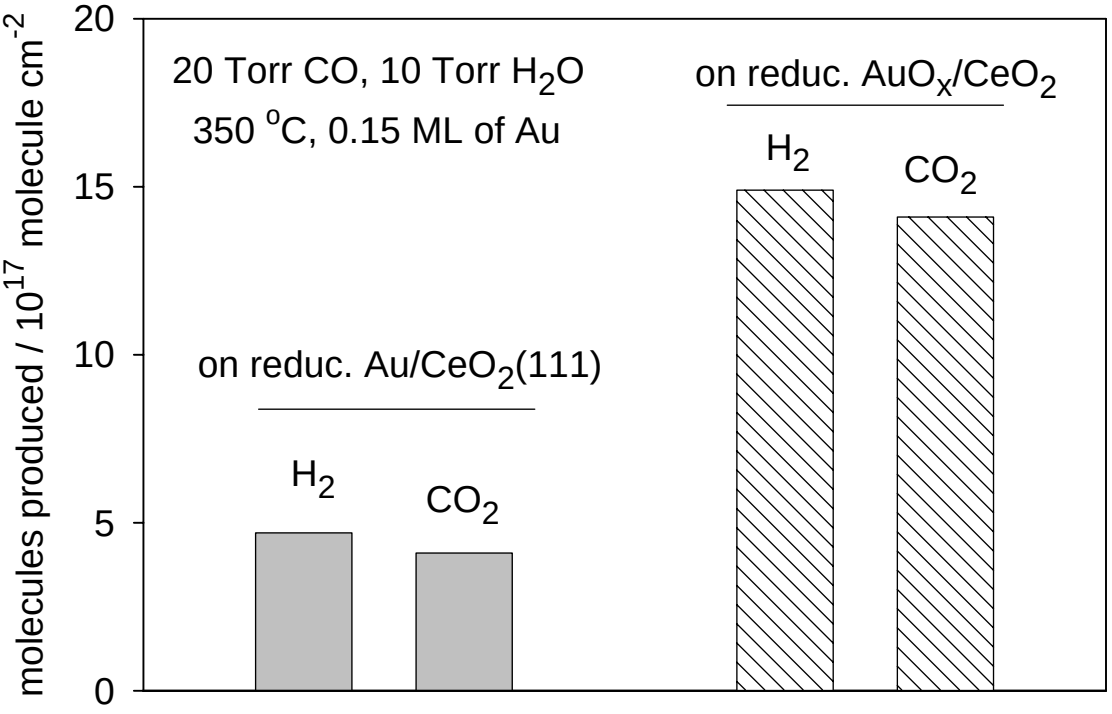
20 Torr CO, 10 Torr H2O
350 oC, 0.15 ML of Au
on reduc. AuOx/CeO2
H2
CO2
on reduc. Au/CeO2(111)
H2
CO2
molecules produced / 10^17 molecule cm^-2
0
5
10
15
20

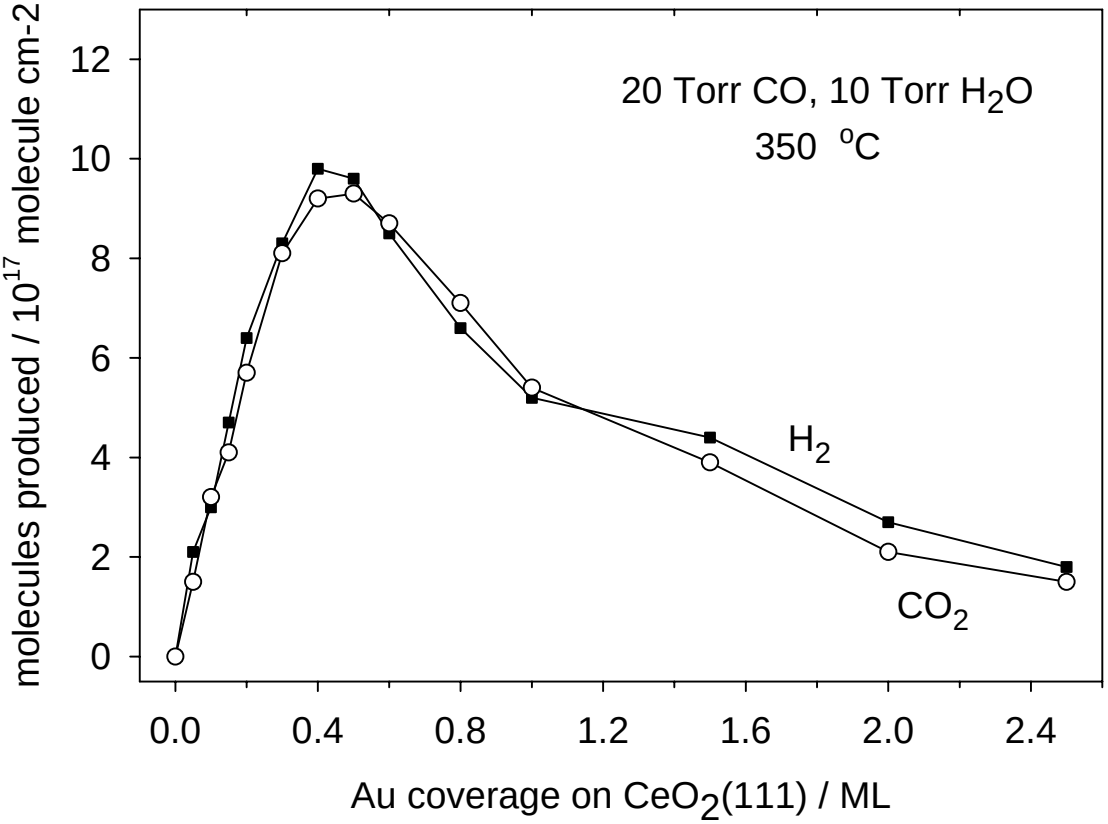
20 Torr CO, 10 Torr H2O
350 oC
H2
CO2
molecules produced / 10^17 molecule cm-2
0
2
4
6
8
10
12
0.0
0.4
0.8
1.2
1.6
2.0
2.4
Au coverage on CeO2(111) / ML

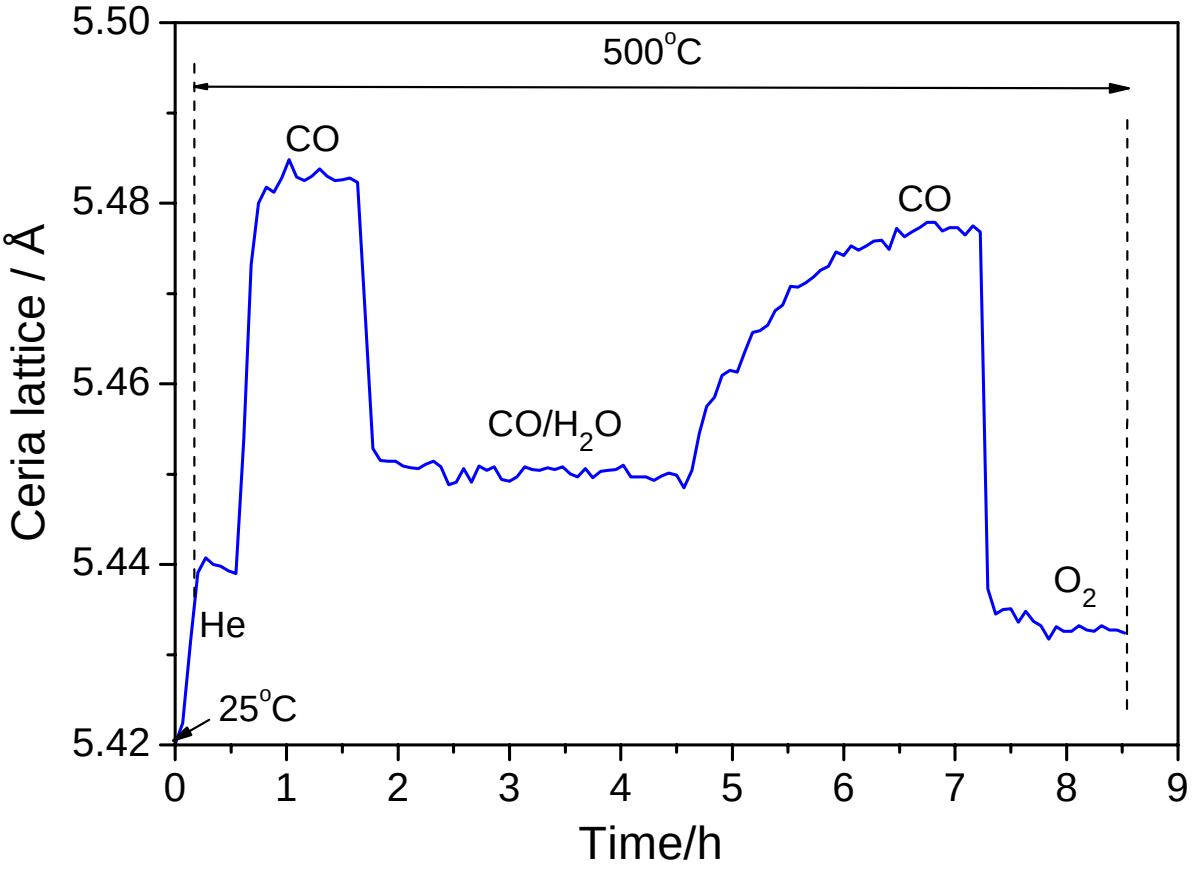
5.50
5.48
5.46
5.44
5.42
Ceria lattice / Å
0
1
2
3
4
5
6
7
8
9
Time/h
500°C
CO
CO
CO/H2O
He
25°C
O2

Fig. 14

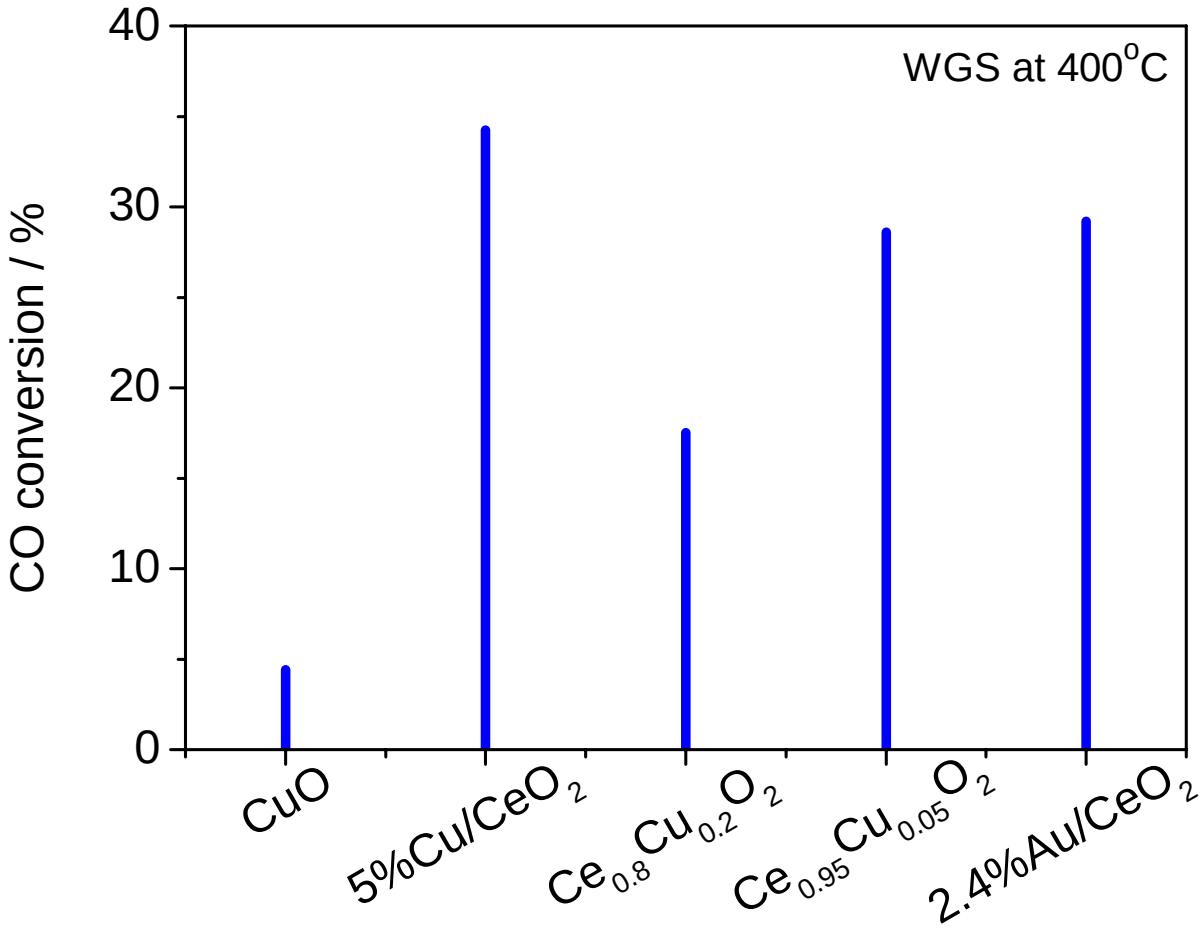
WGS at 400°C
CO conversion / %
40
30
20
10
0
CuO
5%Cu/CeO2
Ce0.8Cu0.2O2
Ce0.95Cu0.05O2
2.4%Au/CeO2

Fig.15

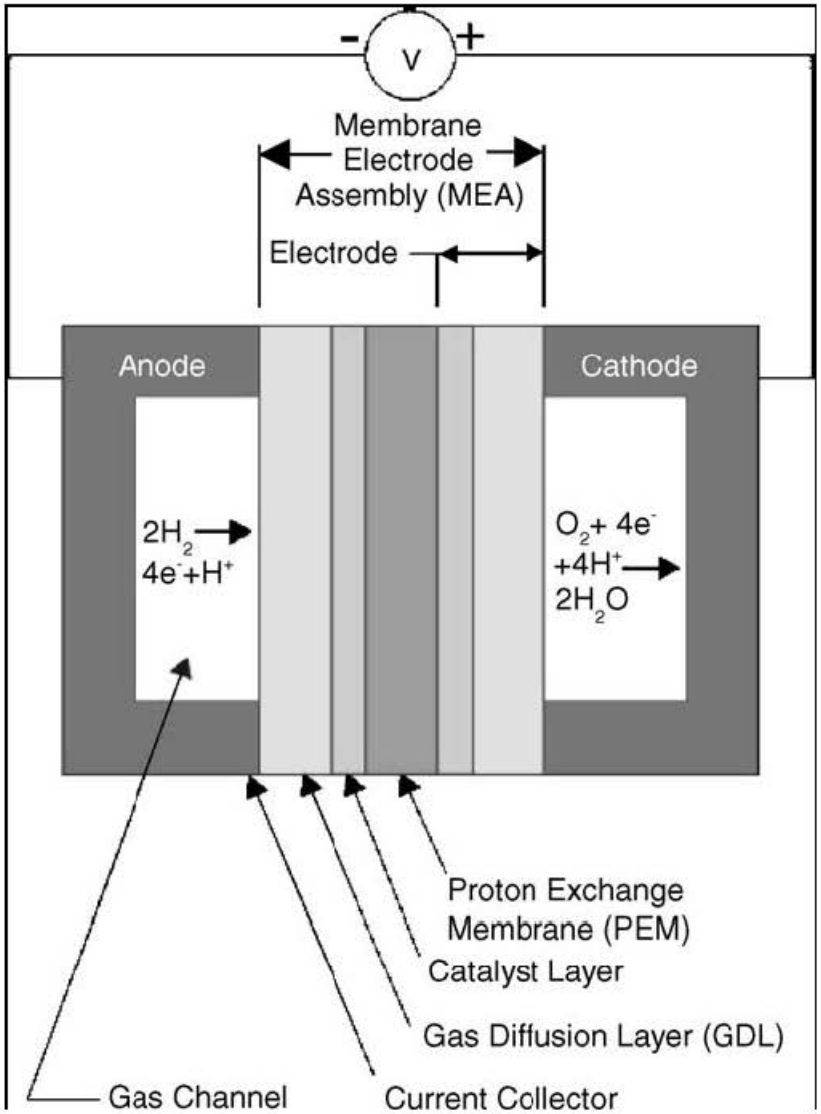
-
V
+
Membrane
Electrode
Assembly (MEA)
Electrode
Anode
Cathode
2H2
4e-+H+
O2+ 4e-
+4H+
2H2O
Proton Exchange
Membrane (PEM)
Catalyst Layer
Gas Diffusion Layer (GDL)
Gas Channel
Current Collector

Fig.16

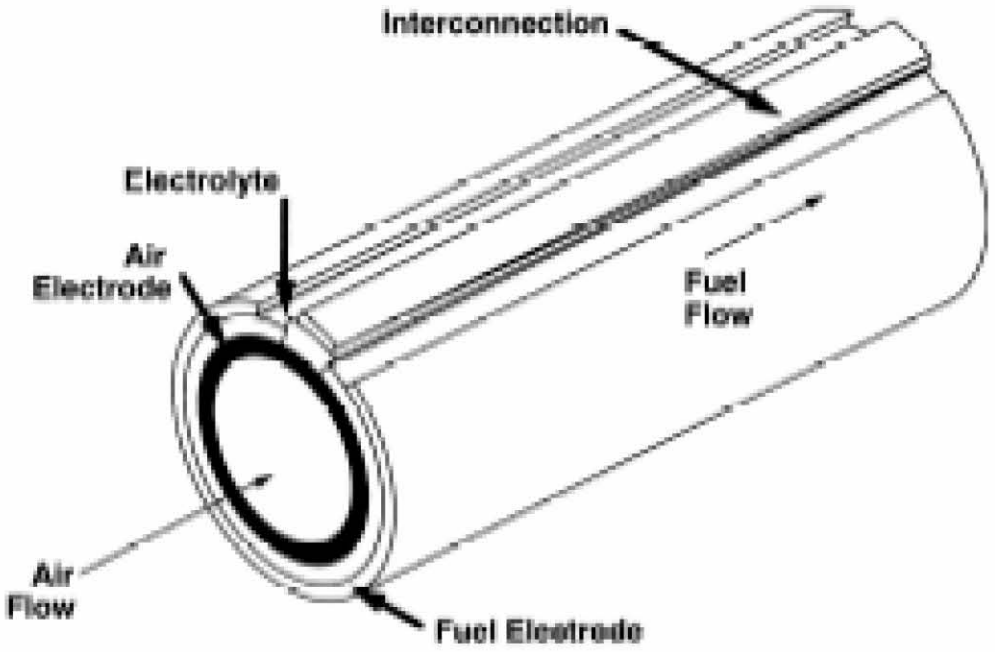
Interconnection
Electrolyte
Air
Electrode
Fuel
Flow
Air
Flow
Fuel Electrode

Fig.17